T.C. Blanken et al.

Control-oriented modeling of the plasma particle density in tokamaks and application to real-time density profile reconstruction

Control-oriented modeling of the plasma particle density in tokamaks and application to real-time density profile reconstruction

T.C. Blanken[1,2], F. Felici[1], C.J. Rapson[3], M.R. de Baar[1,2], W.P.M.H. Heemels[1], the TCV team[4] and the ASDEX-Upgrade team[3]

[1] Eindhoven University of Technology, Faculty of Mechanical Engineering, Control Systems Technology Group, P.O. Box 513, 5600 MB Eindhoven, The Netherlands.
[2] FOM-institute DIFFER - Dutch Institute for Fundamental Energy Research, Association EURATOM-FOM, P.O. Box 6336, 5600 HH Eindhoven, The Netherlands.
[3] Max-Planck-Institut für Plasmaphysik, Garching, Germany.
[4] École Polytechnique Fédérale de Lausanne (EPFL), Swiss Plasma Center, Lausanne, Switzerland.

E-mail: `t.c.blanken@tue.nl`

Abstract. A model-based approach to real-time reconstruction of the particle density profile in tokamak plasmas is presented, based on a dynamic state estimator. Traditionally, the density profile is reconstructed in real-time by solving an ill-conditioned inversion problem using a measurement at a single point in time. This approach is sensitive to diagnostics errors and failure. The inclusion of a dynamic model in a real-time estimation algorithm allows for reliable reconstruction despite diagnostic errors. Predictive simulations show that the model can reproduce the density evolution of discharges on TCV and ASDEX-Upgrade after tuning of a few parameters. Offline reconstructions using experimental data from TCV show accurate estimation of the density profile and show examples of fault detection of interferometry signals.

1. Introduction

A key challenge in tokamak operations is maintaining stable plasma conditions, remaining within safety limits and accurate control of the plasma state [1]. Plasma control has expanded in recent years from control of bulk plasma quantities (such as total plasma current, average particle density and average temperature) to control of the spatial distributions of these quantities, for example the temperature and safety factor profiles [2–5].

Since the density profile affects the plasma pressure and fusion power [6], drives radiation, influences the non-inductive current distribution, determines diagnostics validity (e.g. ECE cut-off), and can trigger detrimental plasma instabilities [7, 8], real-time monitoring and control of the particle density profile is of great importance for safe, reliable and high-performance operation of large tokamaks such as ITER [9–12]. An important challenge can be identified as to enable density control, namely the reliable real-time reconstruction of the density profile from diagnostic measurements.

Most tokamaks have diagnostics for the plasma particle density that can be used for monitoring and real-time control. Often an interferometry system is used, which measures the line-integrated electron density along one or more laser chords intersecting the plasma [13, 14], but other possibilities include Thomson scattering [13, 15] and reflectometry [13, 16].

In control and monitoring of the density, the line-averaged density is often considered, which is conveniently derived from an interferometry signal if the chord intersection length is known. Moreover, there exist data fitting methods for reconstruction of the density profile for analysis or control that minimize a least-squares criterium or fit splines on multiple interferometry channels [17–23] or Thomson

scattering [24, 25] at one point in time. However, the estimates obtained by these static data fitting methods are sensitive to diagnostic faults [17, 26], notably drifts. For example fringe jumps occur in an interferometry system if the density fluctuates rapidly, often when a pellet is injected. This may result in a loss of control performance or even a loss of density control. Despite ongoing research on detection and correction of fringe jumps [18, 26–28], no reliable solution is being used on TCV and ASDEX-Upgrade. Moreover, data fitting methods can suffer from ill-conditioning, leading to unrealistic profiles with spatial oscillations [17].

The inclusion of a dynamic model of the density profile evolution in the profile reconstruction may solve these issues by promoting proximity of the measured quantities to solutions that are feasible with respect to our knowledge of the modeled process. Thereby it can suppress unrealistic spatial oscillations in the profile estimate, reject measurement noise and anticipate for the effects of actuation, such as fuelling, on the density evolution.

For this purpose, we present a control-oriented model of the plasma particle density evolution. We prefer a white-box model-based approach over identifying models from data since nonlinear behaviour and physical couplings that evolve in time complicate identification of processes from measurement data. On the other hand, full first-principle physics modeling is challenging since

(i) transport inside a tokamak plasma LCFS is modeled by the combination of a set of 1D PDEs for radial transport and a 2D elliptical PDE for the magnetic equilibrium (see [29, 30]) which is difficult and time-consuming to solve in combination with calculation of the particle fluxes, and

(ii) transport outside the tokamak plasma LCFS consists of complex processes such as

wall retention and recycling, neutral particle dynamics, and atomic and molecular processes (see [6, 31]) which are all complex to model in themselves, let alone in their interaction.

Because of these complications, heuristic models are better suited for real-time applications in this case. We present a control-oriented and real-time nonlinear model for radial (1D) plasma density transport with additional particle inventories (0D) of the wall and vacuum. Compared to existing multi inventory (0D) models for density control [25, 32–37], we replace the plasma particle inventory by the spatial distribution of the plasma density. Moreover, we include the influence of plasma equilibrium, temperature, current and operational modes (limited or diverted plasma, low or high confinement [6]) on the transport processes and diagnostics.

We propose in this paper to use a model-based dynamic state observer, also known as a Kalman filter [38], to provide real-time estimates of the density profile as well as systematic model deviations from multiple diagnostics signals for the purpose of feedback control. Here we build upon earlier work in [39, 40], where physics-model-based dynamic state observers have been applied for real-time estimation of the current and temperature profiles. In the observer, we employ a threshold method to detect fringe jumps [26], from the discrepancy between the measured interferometry signals and the model-based predictions of these measurements.

The proposed solution can be implemented on existing tokamaks. For future tokamaks as ITER, this model-based design procedure can be performed today with models extrapolated from existing tokamaks and iterated using the same methodology as density transport parameters become better known in the course of ITER operation. We want to emphasize that the purpose of this paper is not to make statements on the physics of density evolution in tokamaks. Instead, the objective is to demonstrate

that a control-oriented model can be used to enhance real-time reconstruction of the density profile.

The remainder of this paper is structured as follows. The control-oriented model of the density transport is introduced in Section 2, along with simulations of a TCV and an ASDEX-Upgrade discharge. The design of the observer, the detection of fringe jumps and the offline estimation results on experimental data are discussed in Section 3. Extensions and future work that is in line with the proposed solutions are discussed in Section 4. Finally, concluding remarks are given in Section 5.

2. Control-oriented 0+1D model of the particle transport

In this section, a 0D+1D diffusion/drift transport model is presented for control purposes, with the flexibity to adapt for multiple devices, multiple diagnostics and multiple actuators. Particle transport in the plasma, particle flows and sources in the tokamak are modeled in a heuristic fashion, rather than using complex first-principle transport models.

Existing physics models of plasma particle transport (e.g. [41, 42]) and models used in offline profile reconstruction algorithms (e.g. ASTRA [30], CRONOS [43]) are not directly suitable for the task of real-time density reconstruction, since their execution time generally exceeds the discharge duration. It has been shown in [2–5, 39, 40] that low-complexity 1D models can be used for reconstruction and control of the temperature and safety factor profiles.

Our model consists of a 1D drift-diffusion PDE for radial particle transport and two 0D ODEs for the time evolution of the inventory of the wall and the neutral vacuum, all based on particle conservation laws. This approach is similar to multi inventory (0D) models for controller design on TCV [34], JET [35], TEXT [33] and

KSTAR [36], but here the radial particle transport in the plasma is also modeled. Since transport on flux surfaces is several orders of magnitude faster than radial transport (perpendicular to flux surfaces), we may consider radial plasma transport only [29]. The ionization, recombination and recycling terms are approximated, and the NBI and pellet injection deposition locations are postulated. See Figure 1 for a schematic representation of the modeled transport flows considered in this model.

The particle transport processes change in time due to a variety of physical factors. The LCFS electron temperature $T_{\mathrm{e,b}} = T_{\mathrm{e}}|_{\rho=1}$, electrical current I_{p}, plasma geometry through 2D equilibrium $\psi(R,Z)$ and distinct operational regimes (limited or diverted plasma $c_{\mathrm{D}} \in \{0,1\}$, low or high confinement mode $c_{\mathrm{H}} \in \{0,1\}$) are included in the model as a time-varying external input parameter. It is assumed that estimates of these parameter values are available through real-time 2D equilibrium reconstruction and other diagnostics.

The PDE is discretized in space and the resulting set of ODEs is then discretized in time. The relation between plasma density and measured quantities is included using diagnostics models.

2.1. 1D radial plasma transport

Let us start by defining the usual toroidal flux surface label $\rho_{\mathrm{tor}} = \sqrt{\frac{\Phi}{\pi B_0}}$ where Φ is the toroidal magnetic flux and B_0 is the vacuum toroidal magnetic field strength at the major radius R_0, see [29]. By defining $\rho_{\mathrm{tor,B}}$ as ρ_{tor} on the LCFS, a dimensionless flux label ρ can be introduced, given by

$$\rho = \frac{\rho_{\mathrm{tor}}}{\rho_{\mathrm{tor,B}}} \tag{1}$$

The flux-surface average of a quantity Q is defined as $\langle Q \rangle = \frac{\partial}{\partial V} \int Q \, dV$ (see e.g. [30]). We assume a quasi-neutral plasma with a constant effective charge Z_{eff}, but the
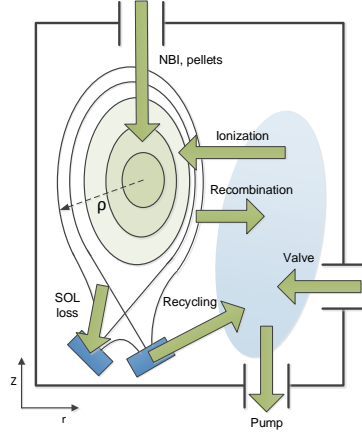
Figure 1. Schematic representation of the tokamak cross-section in the R-Z plane. Depicted are the plasma, the wall components, the neutral vacuum and the modeled particle flows.

methodology may be extended to time-varying Z_{eff} and/or additional particle species.

2.1.1. Electron density continuity The evolution of the flux-surface averaged electron density $n_e(\rho, t)$ resulting from radial transport and a net source is modeled as a PDE [29] on the domain $\Omega = \{(t, \rho) \in \mathbb{R} \mid t_0 \leq t \leq t_{\text{f}}, \ 0 \leq \rho \leq \rho_{\text{e}}\}$.

$$\frac{1}{V'}\frac{\partial}{\partial t}\left(n_e V'\right) + \frac{1}{V'}\frac{\partial \Gamma}{\partial \rho} = S \tag{2}$$

where the constant $\rho_{\text{e}} > 1$ represents the location of the scrape-off layer edge, $\Gamma(\rho, t)$ is the radial electron transport flux, $S(\rho, t)$ is the net electron source and $V' = \frac{\partial V}{\partial \rho}$ with $V(\rho)$ the volume enclosed by a flux surface. Strictly speaking, ρ_{tor} is not defined outside the LCFS due to the open field lines. However, we choose to artificially prolong ρ up to ρ_{e} and we set $\nabla\rho|_{1<\rho\leq\rho_e} := \nabla\rho|_{\rho=1}$ and $V'|_{1<\rho\leq\rho_e} := V'|_{\rho=1}$.

2.1.2. Radial plasma particle flux The radial electron flux $\Gamma(\rho, t)$ is governed by diffusion and a drift (pinch) velocity [29, 44] and is given by

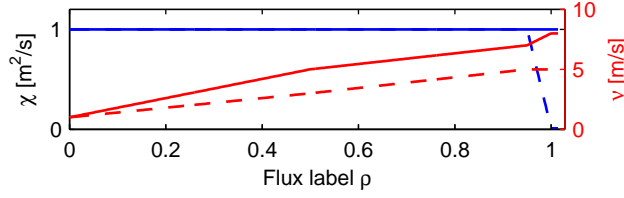$$\Gamma = -V'\left(G_1 D \frac{\partial n_e}{\partial \rho} + G_0 \nu n_e\right) \tag{3}$$

Figure 2. Modeled diffusion D (blue) and drift velocity ν (red) coefficients as a function of ρ. Solid and dashed lines indicate the coefficients for low confinement ($c_H = 0$) and high confinement ($c_H = 1$), respectively.

where D and ν are the coefficients of diffusion and drift (pinch), and $G_1 = \left\langle (\nabla \rho)^2 \right\rangle$, $G_0 = \langle |\nabla \rho| \rangle$ and $\langle |\nabla \rho| \rangle = \langle |\nabla \psi| \rangle \left(\frac{\partial \psi}{\partial \rho} \right)^{-1}$ are geometrical parameters that depend on the $\psi(R, Z)$ equilibrium [29]. The values for D and ν are estimated to represent the empirical system behaviour. Thus, $D(\rho, c_H)$ and $\nu(\rho, I_p, c_H)$ are chosen as simple functions of ρ and c_H, and it is assumed that $\nu = \nu_0 \frac{I_p}{I_{p,0}}$ to represent the increase of pinch at higher current, where $I_{p,0}$ is the *nominal* plasma current. An H-mode implies a reduction of transport in the plasma edge [45] and is reproduced by lower edge diffusion and a lower drift velocity for $c_H = 1$. In Figure 2, the chosen functions $D(\rho, c_H)$ and $\nu(\rho, I_{p,0}, c_H)$ are depicted for both L- and H-mode.

2.1.3. Domain and boundary conditions The domain edge ρ_e is chosen as $\rho_e = 1 + \lambda_{SOL}$ where the dimensionless scrape-off layer width λ_{SOL} is constant and estimated a priori as $\lambda_{SOL} = \sqrt{D|_{\rho=1, c_H=0} \, \pi R_0 q_{95} c_s^{-1}}$ [6, 31], where q_{95} is the *nominal* edge safety factor at 95% of the normalized poloidal flux and c_s is the ion velocity at *nominal* scrape-off layer temperature. The boundary conditions are $\left. \frac{\partial n_e}{\partial \rho} \right|_{\rho=0} = 0$ and $n_e|_{\rho=\rho_e} = 0$. The outflux at the domain edge $\Gamma|_{\rho=\rho_e}$ is treated as a source to the vacuum inventory.

2.1.4. Sources In our model the source is composed of four parts and is written as

$$S = S_{\text{inj}} + S_{\text{iz}} - S_{\text{rec}} - S_{\text{SOL}\rightarrow\text{wall}} \tag{4}$$

These four contributions are depicted in Figure 1 and are modeled as follows.

- The electron source of ionization of injected neutrals from NBI and pellets is modeled by their particle deposition locations, and is given by

$$S_{\text{inj}} = \Lambda_{\text{NBI}}(\rho)\,\Gamma_{\text{NBI}}(t) + \Lambda_{\text{pellet}}(\rho)\,\Gamma_{\text{pellet}}(t) \tag{5}$$

  where Γ_{NBI} and Γ_{pellet} are the NBI and pellet injection fuelling rates. The functions $\Lambda_{\text{NBI}}(\rho)$ and $\Lambda_{\text{pellet}}(\rho)$ model the spatial deposition of the ionization of injected neutrals, with $\int_{V_{\text{p}}} \Lambda_{\text{NBI}} dV = \int_{V_{\text{p}}} \Lambda_{\text{pellet}} dV = 1$ such that $\int_{V_{\text{p}}} S_{\text{inj}} dV = \Gamma_{\text{NBI}} + \Gamma_{\text{pellet}}$.

- The electron source thermal ionization of other neutrals equals $\langle \sigma v \rangle_{\text{iz}}\, n_n n_e$ where $\langle \sigma v \rangle_{\text{iz}}(T_{\text{e}})$ is the ionization cross-section [6] and n_n is the neutral density, but is approximated as

$$S_{\text{iz}} = \langle \sigma v \rangle_{\text{iz}}(T_{\text{e,b}})\, \Lambda_{\text{iz}} \frac{N_{\text{v}}}{V_{\text{v}}} n_e \tag{6}$$

  where $T_{\text{e,b}} = T_{\text{e}}|_{\rho=1}$ is the LCFS electron temperature, N_{v} is the vacuum inventory, $V_{\text{v}} = V_{\text{r}} - V_{\text{p}}$ is the vacuum volume, V_{r} is the vessel volume and V_{p} is the plasma volume. The function $\Lambda_{\text{iz}}(\rho, c_{\text{D}})$ models the product of the spatial distribution of the neutral density and the ionization cross-section such that $\langle \sigma v \rangle_{\text{iz}}(T_{\text{e,b}})\, \Lambda_{\text{iz}} \frac{N_{\text{v}}}{V_{\text{v}}} \approx \langle \sigma v \rangle_{\text{iz}}(T_{\text{e}})\, n_n$.

- The thermal recombination sink of ions equals $\langle \sigma v \rangle_{\text{rec}}\, n_e n_i$ where $\langle \sigma v \rangle_{\text{rec}}(T_{\text{e}})$ is the recombination cross-section [6] and n_i is the ion density, but is approximated as

$$S_{\text{rec}} = \langle \sigma v \rangle_{\text{rec}}(T_{\text{e,b}})\, \Lambda_{\text{rec}} n_e^2 \tag{7}$$

  The function $\Lambda_{\text{rec}}(\rho)$ models the spatial distribution of the recombination cross-section such that $\langle \sigma v \rangle_{\text{rec}}(T_{\text{e,b}})\, \Lambda_{\text{rec}} \approx \langle \sigma v \rangle_{\text{rec}}(T_{\text{e}})$.
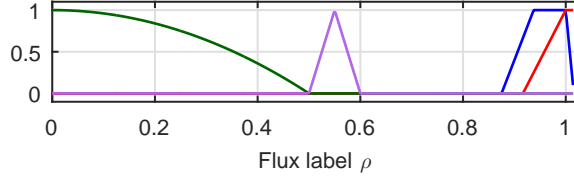
Figure 3. Example of spatial distributions Λ_{iz} (blue), Λ_{rec} (red), Λ_{NBI} (green) and Λ_{pellet} (magenta) for a limited plasma.

- The particle sink in the scrape-off layer due to wall impact of particles exiting the plasma through the scrape-off layer is modeled as

$$S_{\text{SOL}\to\text{wall}} = \frac{H(\rho - 1)\, n_e}{\tau_{\text{SOL}}} \tag{8}$$

where $H(\cdot)$ is the Heaviside function and $\tau_{\text{SOL}}(c_{\text{D}})$ is the time constant for particle loss through the scrape-off layer [31], modeled as

$$\tau_{\text{SOL}} = \begin{cases} \pi R_0 q_{95} c_s^{-1} & \text{if } c_{\text{D}} = 0 \\ \\ g_{\text{d}} \pi R_0 q_{95} c_s^{-1} & \text{if } c_{\text{D}} = 1 \end{cases}$$

where $g_{\text{d}} > 1$ is used to model the reduction of net outflow to the wall in a diverted plasma.

The functions Λ_{iz}, Λ_{rec}, Λ_{NBI} and Λ_{pellet} are chosen ad-hoc in this study, see Figure 3, but could be computed using more detailed physics models of e.g. neutral beam injection [46, 47]. The width of $\Lambda_{\text{iz}}(\rho, c_{\text{D}})$ is decreased for $c_{\text{D}} = 1$ to model the decreased ionization depth experienced in a diverted plasma, where the main plasma is located farther from the wall components due to flux expansion.

2.2. 0D model of the neutral wall inventory

All particles in the tokamak that are not in the plasma are either assigned to the wall inventory $N_{\text{w}}(t)$ or the neutral vacuum inventory $N_{\text{v}}(t)$. The wall inflow is formed by the scrape-off layer sink $S_{\text{SOL}\to\text{wall}}$ and the outflow is denoted by $\Gamma_{\text{recycle}}(t)$, see

Figure 1. The wall particle inventory balance is given by

$$\frac{dN_{\mathrm{w}}}{dt} = \Gamma_{\mathrm{SOL}\rightarrow\mathrm{wall}}(t) - \Gamma_{\mathrm{recycle}}(t) \tag{9}$$

where $\Gamma_{\mathrm{SOL}\rightarrow\mathrm{wall}} = \int_{V_{\mathrm{p}}} S_{\mathrm{SOL}\rightarrow\mathrm{wall}}dV$. The wall recycling outflow $\Gamma_{\mathrm{recycle}}(t)$ is modeled by a linear term representing outward diffusion of particles embedded in the wall material and a term representing particle expulsion due to impacting plasma particles. Hereby, the latter outflow matches the inflow from the scrape-off layer if the wall inventory N_{w} approaches the saturation level N_{sat}, and is given by

$$\Gamma_{\mathrm{recycle}} = \frac{N_{\mathrm{w}} - c_w V_{\mathrm{v},0} V_{\mathrm{v}}^{-1} N_{\mathrm{v}}}{\tau_{\mathrm{release}}} + \frac{N_{\mathrm{w}}}{N_{\mathrm{sat}}} \Gamma_{\mathrm{SOL}\rightarrow\mathrm{wall}} \tag{10}$$

where $V_{\mathrm{v},0} = V_{\mathrm{r}} - V_{\mathrm{p},0}$ is the *nominal* vacuum volume, $V_{\mathrm{p},0}$ is the *nominal* plasma volume and τ_{release} is a time constant for the decay of the wall inventory due to outward diffusion, c_w is a dimensionless constant that determines the steady-state balance between the wall inventory and vacuum density, and $N_{\mathrm{sat}}(c_{\mathrm{D}}, c_{\mathrm{H}})$ is the saturation level of the wall inventory, modeled as

$$N_{\mathrm{sat}}(c_{\mathrm{D}}, c_{\mathrm{H}}) = \begin{cases} N_{\mathrm{sat},0} & \text{if } c_{\mathrm{D}} = 0,\ c_{\mathrm{H}} = 0 \\ N_{\mathrm{sat},\mathrm{D}} & \text{if } c_{\mathrm{D}} = 1,\ c_{\mathrm{H}} = 0 \\ N_{\mathrm{sat},\mathrm{H}} & \text{if } c_{\mathrm{D}} = 1,\ c_{\mathrm{H}} = 1 \end{cases}$$

where $N_{\mathrm{sat},\mathrm{D}} > N_{\mathrm{sat},0}$ to model the absorption of particles by the wall when the plasma is diverted and $N_{\mathrm{sat},\mathrm{H}} < N_{\mathrm{sat},\mathrm{D}}$ to model the expulsion of wall particles when the plasma enters an H-mode [48]. The coefficients $N_{\mathrm{sat},0}$, $N_{\mathrm{sat},0}$, $N_{\mathrm{sat},0}$, $\tau_{release}$ and c_{wv} are difficult to obtain from data, since no diagnostics exist to measure the wall inventory, and retention and recycling depend on the wall conditioning. However, they can be estimated using studies that identify retention [49, 50].

2.3. 0D model of the neutral vacuum inventory

The particle inflows to the vacuum are the thermal recombination S_{rec}, wall recycling outflow Γ_{recycle} and gas injection Γ_{valve}, see Figure 1. We also include the plasma outflux at the domain edge $\Gamma|_{\rho=\rho_e}$. The outflows from the vacuum are the ionization S_{iz} and the (cryo)pump outflow Γ_{pump}. The vacuum particle inventory balance is given by

$$\frac{dN_{\text{v}}}{dt} = \Gamma_{\text{rec}}(t) - \Gamma_{\text{iz}}(t) + \Gamma|_{\rho=\rho_e}$$
$$+ \Gamma_{\text{recycle}}(t) + \Gamma_{\text{valve}}(t) - \Gamma_{\text{pump}}(t) \tag{11}$$

where $\Gamma_{\text{rec}} = \int_{V_{\text{p}}} S_{\text{rec}} dV$ and $\Gamma_{\text{iz}} = \int_{V_{\text{p}}} S_{\text{iz}} dV$. The (cryo)pump outflow $\Gamma_{\text{pump}}(t)$ is assumed to be proportional to the neutral density and is given by

$$\Gamma_{\text{pump}} = \frac{N_{\text{v}} V_{\text{v},0}}{\tau_{\text{pump}} V_{\text{v}}} \tag{12}$$

where τ_{pump} is a time scale that expresses exponential decay of the neutral density due to pumping, which may depend on the number of pumps used and the strike point positions.

2.4. Inputs

The gas inflow rate $\Gamma_{\text{valve}}(t)$, NBI fuelling rate $\Gamma_{\text{NBI}}(t)$ and pellet fuelling rate $\Gamma_{\text{pellet}}(t)$ are considered as inputs to the system. They are constrained to be nonnegative and have upper limits, expressed as

$$0 \leq \Gamma_{\text{valve}}(t) \leq \Gamma_{\text{valve}}^{\max} \tag{13a}$$

$$0 \leq \Gamma_{\text{NBI}}(t) \leq \Gamma_{\text{NBI}}^{\max} \tag{13b}$$

We assume that the gas inflow rate $\Gamma_{\mathrm{valve}}(t)$ is either proportional to the actuator input signal, or that the gas valve is feedback controlled to provide the flow $\Gamma_{\mathrm{valve}}(t)$. The pellet injection fuelling rate $\Gamma_{\mathrm{pellet}}(t)$ is a pulsed signal which takes on either zero or $\Gamma_{\mathrm{pellet}}^{\mathrm{max}}$. Each pulse represents the arrival of an individual pellet and the time integral of each pulse equals the number of deposited electrons.

2.5. External input parameter

The coefficients of the model change in time due to a variety of external factors. These are modeled by a time-varying external input parameter $p(t)$, defined as

$$p = \begin{bmatrix} c_{\mathrm{D}} & c_{\mathrm{H}} & T_{\mathrm{e,b}} & I_{\mathrm{p}} & V' & G_1 & G_0 & \Omega \end{bmatrix} \tag{14}$$

where $T_{\mathrm{e,b}} = T_{\mathrm{e}}|_{\rho=1}$ is the electron temperature at the LCFS, Ω is a matrix that links the density profile to the diagnostic outputs and is introduced in Section 2.8, and V', G_1, G_0, and Ω are determined from an equilibrium $\psi(R, Z)$. We assume that the parameter values are available through real-time equilibrium reconstruction (see e.g. [51–53]) and/or diagnostics.

2.6. Spatial discretization using finite elements

The numerical solution of (2), (9) and (11) is implemented using a finite element method (see e.g. [54]) for the spatial discretization similar to [55] and a trapezoidal method for the time discretization. The methodology describing the use of finite elements and the time discretization are discussed in detail in Appendix A.1 and Appendix A.2 respectively, but a brief outline is given here.

First, the electron density is approximated as

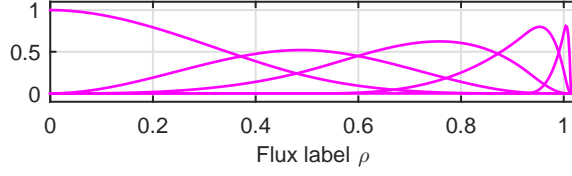$$n_e(\rho, t) = \sum_{\alpha=1}^{m} \Lambda_\alpha(\rho) b_\alpha(t) \tag{15}$$

Figure 4. Example of basis functions $\Lambda_\alpha\left(\rho\right),\ \alpha\ =\ 1, 2, ..., m$ with $m = 5$ used to spatially discretize the electron density (15).

where the basis functions $\Lambda_\alpha : \left[0, \rho_{\mathrm{e}}\right] \rightarrow \left[0, 1\right],\ \alpha = 1, 2, ..., m$ are chosen as cubic B-splines with finite support [56]. B-splines are continuous and differentiable piecewise polynomials on a finite domain [56]. An example set of basis functions is shown in Figure 4. The variables $b\left(t\right) = \begin{bmatrix} b_1\left(t\right) & \cdots & b_m\left(t\right) \end{bmatrix}^T$ are the time-varying spline coefficients. For the purpose of control-oriented modeling, a small number of basis functions ($m = 5$) with closely-spaced spline knots around the plasma edge is chosen. The boundary conditions discussed in Subsection 2.1.3 are imposed by restricting the values and derivatives of the basis functions at the boundaries.

Second, an equidistant time discretization $t_k = t_0 + kT_{\mathrm{s}},\ k = 0, 1, ..., N$ is chosen, where $T_{\mathrm{s}} > 0$ is the time step and $N = \left(t_{\mathrm{f}} - t_0\right)/T_{\mathrm{s}}$.

Finally, applying the finite element method and the trapezoidal time discretization on (2), (9) and (11) as described in Appendix A.1 and Appendix A.2 yields the system of nonlinear discrete-time ODEs

$$x_k = f_{\mathrm{d}}\left(p_{k-1}, x_{k-1}\right) + B_{\mathrm{d}}\left(p_{k-1}\right)u_{k-1} \tag{16}$$

where $p_k = p\left(t_k\right)$, and the state $x_k \in \mathbb{R}^{n_x}$ and the input $u_k \in \mathbb{R}^{n_u}$ are defined as

$$x_k = \begin{bmatrix} b\left(t_k\right) \\ N_{\mathrm{w}}\left(t_k\right) \\ N_{\mathrm{v}}\left(t_k\right) \end{bmatrix} \qquad u_k = \begin{bmatrix} \Gamma_{\mathrm{valve}}\left(t_k\right) \\ \Gamma_{\mathrm{NBI}}\left(t_k\right) \\ \Gamma_{\mathrm{pellet}}\left(t_k\right) \end{bmatrix}$$

with $n_x = m + 2$ and $n_u = 3$. Because of the products of n_e, N_{w} and N_{v} in (6), (7)

and (10), $f_{\mathrm{d}}\left(p_{k}, x_{k}\right)$ is a nonlinear function of x_{k}.

2.7. Interferometry measurements

The interferometry output signal is proportional to the line-integrated electron density along a laser chord intersecting the plasma (see e.g. [13]). Multiple chords with different line of sight through the plasma allow to infer the electron density profile. The interferometry phase signal $\Delta\phi$ of the c-th chord at the sampling time instant t_k is denoted by $\Delta\phi_k^c \in \mathbb{R}$ and is given by

$$\Delta\phi_k^c = c_{FIR} \int_{L_c} n_e\left(\rho\left(\psi\left(R, Z\right)\right), t_k\right) dL \tag{17}$$

where L_c is the intersection length of the plasma and the c-th laser chord, and the interferometry constant is given by $c_{FIR} = \lambda e^2 / \left(4\pi\epsilon_0 m_e c^2\right)$ where λ is the laser wavelength, e is the electron charge, ϵ_0 is the the permittivity of vacuum, m_e is the electron rest mass and c is the speed of light.

2.7.1. Modeling fringe jumps
Fringe jumps are counting errors of the interferometry phase difference $\Delta\phi$ and form infrequent jumps at individual output channels. While fringe jumps are infrequent, their magnitude is sufficiently large to disturb density estimates and reconstructions. The jump magnitude in the phase signal equals an integer multiple of 2π, i.e. $2\pi k$ $k \in \mathbb{N}$. By incorporating a description of fringe jumps in the measurement, (17) is replaced by

$$\Delta\phi_k^c = c_{FIR} \int_{L_c} n_e\left(\rho\left(\psi\left(R, Z\right), t_k\right)\right) dL + 2\pi d_k^c \tag{18}$$

$$d_k^c = d_{k-1}^c + \Delta_{k-1}^c \tag{19}$$

where $d_k^c \in \mathbb{N}$ is the cumulative number of fringe jumps on chord c at time t_k and $\Delta_{k-1}^c \in \mathbb{N}$ is a stochastic variable that represents possibly multiple jumps on chord c

between time t_{k-1} and t_k.

The probability of jumps is known to be strongly correlated with fast changes of the plasma density [18, 28], but obtaining the probability density function for Δ_k^c as a function of (the time derivative of) the plasma density is beyond the scope of this paper. For the present purposes, it is assumed that initially $d_1^c = 0$ and that the expected value $\mathbb{E}[\Delta_k^c] = 0$.

2.8. Output equation

The measurement output vector of all n_{FIR} available interferometry chords can, by stacking (18), be represented as $y_k \in \mathbb{R}^{n_{FIR}}$ and is given by

$$y_k = \begin{bmatrix} \int_{L_1} n_e(\rho, t_k)\, dL \\ \vdots \\ \int_{L_{n_{FIR}}} n_e(\rho, t_k)\, dL \end{bmatrix} + \delta d_k \tag{20}$$

where $\delta = 2\pi c_{FIR}^{-1}$ and $d_k = \begin{bmatrix} d_k^1 & \cdots & d_k^{n_{FIR}} \end{bmatrix}^T \in \mathbb{N}^{n_{FIR}}$ is the column of the cumulative number of fringe jumps on all chords at time t_k. The fringe jump state equation of all chords is given by

$$d_k = d_{k-1} + \Delta_{k-1} \tag{21}$$

where $\Delta_k = \begin{bmatrix} \Delta_k^1 & \cdots & \Delta_k^{n_{FIR}} \end{bmatrix}^T \in \mathbb{N}^{n_{FIR}}$.

The numerical evaluation of the line integrals is discussed in Appendix A.3. The spatial discretization (15) and an equilibrium $\psi(R, Z)$ allow to express the line integrals in (20) as a linear combination of the electron density spline coefficients b_k from (15). By evaluating the line integrals, the output equation is written as

$$y_k = C(p_k)\, x_k + \delta d_k \tag{22}$$

where $C\left(p_k\right) = \left[\begin{array}{cc} \Omega\left(p_k\right) & 0^{n_{FIR}\times 2} \end{array}\right]$ and $\Omega\left(p_k\right)$ is given by

$$\Omega_{ij}\left(p_k\right) = \int_{L_i} \Lambda_j\left(\rho\left(\psi\left(R, Z\right)\right)\right) dL \qquad (23)$$

It is assumed that $\rho\left(\psi\right)$ and $\psi\left(R, Z\right)$ are known from real-time 2D equilibrium reconstruction (see [51–53]).

2.9. Computational time requirements

For real-time control, a sufficiently high time resolution of at least an order of magnitude larger than the particle confinement time is required. On TCV, the particle confinement time τ_p is at least 10ms [57]. The sampling frequency of the density feedback controller is 1ms on TCV [58] and 1.5ms on ASDEX-Upgrade [18], which is slower than the respective interferometer sampling frequencies [17, 59, 60]. Note that typically, the controller bandwidth used at TCV is below 25Hz [34]. Currently, Thomson scattering measurements of the electron density are not available in real time on TCV and ASDEX-Upgrade. The time resolution of Thomson scattering is limited by the repetition rate of the laser. The repetition rate is in itself typically too low for feedback control, but real-time Thomson scattering measurements may be used to correct the interferometry signals and enhance profile reconstruction.

TCV has a total of 14 interferometry chords, while ASDEX-Upgrade has 6 chords. Presently, the evaluation of (16) and (22) with $n_x = 7$ and $n_{FIR} = 14$ and $T_s = 1$ms, for which details are given in Appendix A.1 through Appendix A.3, takes 2ms of computational time. Here, MATLAB using an Intel$^{®}$Core^{TM}2 DUO E6600 at 2.40 GHz PC running Windows 7 was used. On TCV, the energy confinement time τ_e is between 2ms and 50ms [61–63] and the particle confinement time τ_p from $5\tau_e$ up to $10\tau_e$ [57]. Implementation on a tokamak control system can easily reduce the

computational time to below a cycling time of 1ms, satisfying the required time resolution.

2.10. TCV and ASDEX-Upgrade simulation: qualitative model validation

To validate the model, we present simulations of the model and compare them with measurement data from TCV and ASDEX-Upgrade.

First we use the parameter signals, equilibrium reconstruction and gas valve input signal from TCV shot #41953 as a test case to simulate a TCV discharge. The model coefficients are chosen to be representative for a typical discharge in the TCV tokamak. In Figure 5, the measurements and simulated quantities are shown. The plasma is diverted at $t = 0.33$s and enters a high confinement mode around $t = 0.42$s.

The simulation replicates the measurement with reasonable similarity. The decay of plasma density after the plasma is diverted is not accurately followed: the model assumes an instantaneous change of configuration and transport, whereas the evolution of the strike point location towards their stationary location takes longer. The decay of plasma density therefore takes longer than modeled. Similarly, the rise of plasma density during the low to high confinement mode transition is not accurately followed: again, the model assumes and instantaneous change of transport dynamics, whereas the low to high confinement transition is a more complex process. During flat-top, there is a good agreement between the measurements and the simulated density profile (Fig. 2.1(b)(d)). We emphasize that the ability of the model to produce smooth density profiles is highly valuable for the reconstruction algorithm discussed in the next chapter. Since the wall saturation model (10) is a severe simplification of reality, it is difficult to estimate the coefficients N_{sat} and c_{wv} a priori to predict the absolute value of the plasma density and the wall inventory, both transiently and in flat-top
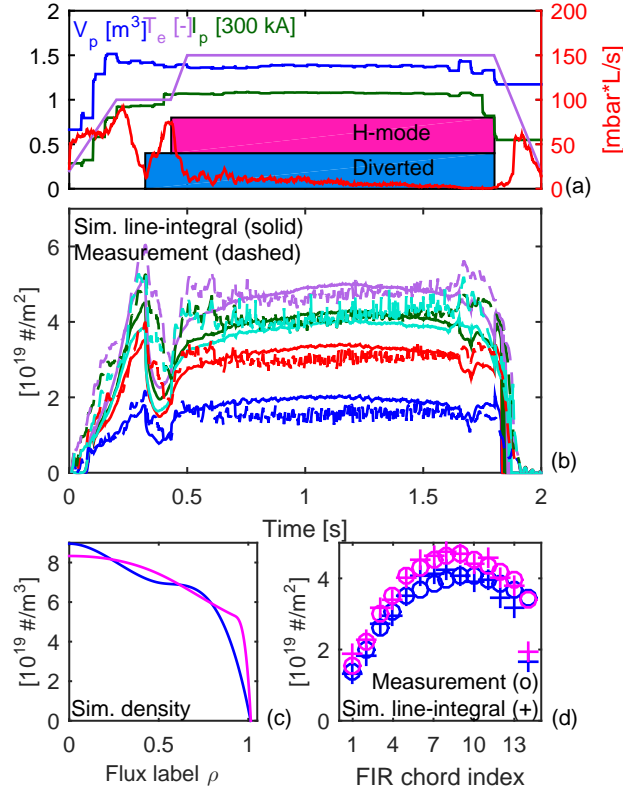
Figure 5. Nominal simulation of TCV plasma using equilibrium and input data from TCV shot #41953 (a). The simulated line-integrated density (solid) and measurements from TCV shot #41953 (dashed) are shown in (b). The simulated density profiles at $t = 0.22$s and $t = 1$s are shown in (c). The simulated line-integrated density and measurement at $t = 0.22$s and $t = 1$s are shown in (c) and (d) respectively.

for various discharge scenarios.

Second, we use the parameter signals, equilibrium reconstruction and input signals from ASDEX-Upgrade shot #32527 as a test case to simulate an ASDEX-Upgrade discharge. The model coefficients are now chosen to be representative for a standard H-mode discharge in ASDEX-Upgrade. In Figure 6, the measurements and simulated quantities are shown. The plasma is diverted at $t = 0.5$s and enters a high confinement mode around $t = 1.8$s.

Here, the simulation replicates the measurements the best during the high

confinement mode. During ramp-up, the density is not well replicated. Since the plasma particle inventory is small compared to the total integrated valve inflow in ASDEX-Upgrade [49, 50], the simulated density is very sensitive to the chosen model equations. Predominantly the wall and pumping models (10),(12) play a large role in the evolution of the plasma density. This can be seen in Figure 6 as the wall inventory approaches 1.8×10^{21} atoms, as was also identified for ASDEX-Upgrade H-mode discharges [49]. However, the density profile at $t = 3$s is replicated with good accuracy and shows the pedestal typically seen in high confinement plasmas. Again, we emphasize that the ability of the model to produce smooth density profiles is highly valuable for the reconstruction algorithm discussed in the next chapter.

3. Dynamic state observer design using Kalman filtering

In this section, the problem of reconstructing the density profile as well as modeling errors/disturbances in real-time is addressed. Here, we will use our knowledge of the process captured in the model, as introduced in Section 2, to complement real-time diagnostics.

We begin this section by introducing the basic working of an observer applied to the density reconstruction problem. Next, a solution to compensate for systematic modeling errors is shown. Subsequently, the observer equations and a method for detecting fringe jumps within the observer from characteristics of this type of sensor error are described. Next, the tuning possibilities and reconstruction tradeoffs of the observer are discussed. At the end of this section, tests of the observer density reconstruction based on simulated data, as well as reconstructions using experimental data are presented.

The dynamic state observer, or Kalman filter [38], is a tool widely used in the
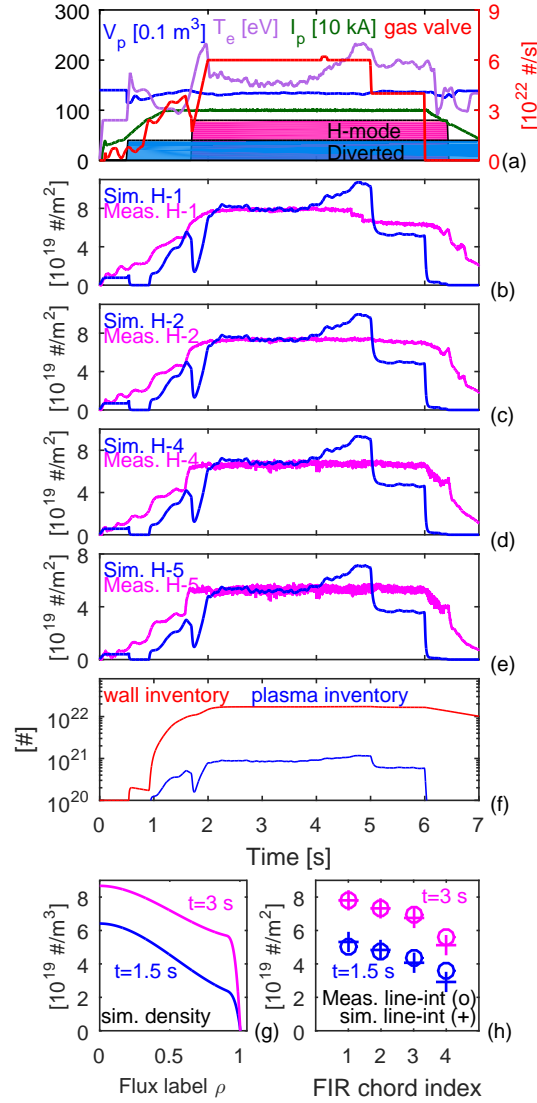
Figure 6. Nominal simulation of an AUG plasma using equilibrium and input data from AUG shot #32527 (a). The simulated line-integrated density (solid) and measurements from AUG shot #32527 (dashed) are shown in (b),(c),(d) and (e) for the five interferometer chords. The simulated wall inventory and plasma inventory are shown in (c). The simulated density profiles at $t = 1.5$s and $t = 3$s are shown in (g). The line-integrated densities and interferometry measurements at $t = 1.5$s and $t = 3$s are shown in (h).

systems & control community [64] for estimating the internal state of a dynamical system in real-time by combining measurements with a model of the system. While a Kalman filter is a minimum-variance estimator for linear dynamical systems, an extended Kalman filter (EKF) is a linearized, and therefore *sub-optimal* version of the Kalman filter for nonlinear dynamical systems [38]. No guarantees can be given about the stability and estimation accuracy of the EKF, but it is considered the *de facto* standard for estimation of nonlinear systems and is widely used [64]. We apply the EKF to estimate the density profile and modeling errors/disturbances in real-time with interferometry diagnostics (17). More specifically, the EKF iteratively produces estimates $\hat{x}_{k|k}$ of the system state x_k at every measurement sample y_k using the state estimate at the previous time step $\hat{x}_{k-1|k-1}$. A block scheme of the proposed dynamic state observer is depicted in Figure 7. At every iteration of the EKF, a one-sample ahead prediction is made based on the nonlinear model (16), (21) and a forward diagnostics model (22) given a state estimate at the previous time step. The state estimate is updated with information from the measurement sample y_k.

The control-oriented model (16), (21), (22) is augmented with an additive random-walk state disturbance to represent modeling errors, similar to [39]. This allows the observer to effectively estimate modeling errors in real-time as systematic differences between measurements and model-based predictions of the measured quantities. The advantage of this method over adapting the model coefficients is that the observer equations remain stable, whereas adaptive parameter estimation methods [65, 66] introduce extra nonlinearity and may be unstable depending on the chosen time step.
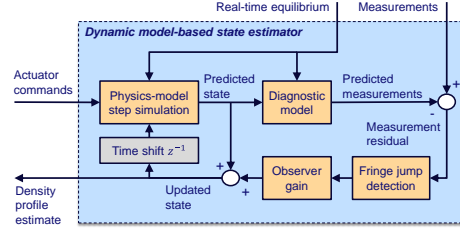
Figure 7. Block diagram of the dynamic state estimator. The state estimator combines measurements with a model to reconstruct the density profile in real-time, to be used for feedback control of the density. We detect fringe jumps from the difference between measurements and model-based predictions of the measured quantities.

3.1. Extended Kalman filter for estimation of state and disturbances

The design of the extended Kalman filter (EKF) [38] including a state disturbance model is now described.

In order to derive the EKF equations we need to model stochastic behavior of our system (16), (22) with associated covariance matrices. First, the diagnostics noise is represented by an additive zero-mean white measurement noise v_k with covariance matrix R_k on the output y_k. Furthermore, uncertainty on the evolution of the density, wall inventory and vacuum inventory is modeled as an additive zero-mean process noise w_k^x with covariance matrix Q_k^x on the state x_k. Finally, additive unknown disturbances $\zeta_k \in \mathbb{R}^m$ are modeled on the plasma density state equation. These disturbances are assumed to be constant $\zeta_{k+1} = \zeta_k$. For estimating these disturbance in the EKF, a white noise signal is added to the evolution equation, yielding $\zeta_{k+1} = \zeta_k + w_k^\zeta$ where w_k^ζ is a zero-mean white noise with covariance matrix Q_k^ζ.

By including these noises and disturbances in our system (16), (21), (22), the augmented system is written as

$$x_k = f_{\mathrm{d}}\left(p_{k-1}, x_{k-1}\right) + B_\zeta \zeta_{k-1} + B_{\mathrm{d}} u_{k-1} + w_{k-1}^x \tag{24a}$$

$$\zeta_k = \zeta_{k-1} + w_{k-1}^{\zeta} \tag{24b}$$

$$d_k = d_{k-1} + \Delta_{k-1} \tag{24c}$$

$$y_k = C\left(p_k\right) x_k + \delta d_k + v_k \tag{24d}$$

where B_ζ is chosen as $B_\zeta = \begin{bmatrix} I^{m\times m} & 0^{m\times 2} \end{bmatrix}^T$ such that each disturbance entry influences one variable of the electron density. Let us define the augmented state $\boldsymbol{x}_k \in \mathbb{R}^{n_x+m}$ as $\boldsymbol{x}_k = \begin{bmatrix} x_k^T & \zeta_k^T \end{bmatrix}^T$ and

$$F_k = \begin{bmatrix} \left.\frac{\partial f_d}{\partial x_k}\right|_{p_k,\hat{x}_{k|k}} & B_\zeta \\ 0 & I^{m\times m} \end{bmatrix} \qquad G = \begin{bmatrix} B_d \\ 0 \end{bmatrix}$$

$$H_k = \begin{bmatrix} C\left(p_k\right) & 0 \end{bmatrix} \qquad Q_k = \begin{bmatrix} Q_k^x & 0 \\ 0 & Q_k^\zeta \end{bmatrix}$$

The EKF equations for the system (24a)-(24d) consist of a prediction and an update step. First, the predicted augmented state $\hat{\boldsymbol{x}}_{k|k-1}$, the predicted fringe jump state $\hat{d}_{k|k-1}$ are based on a forward evaluation of the dynamics (24a)-(24c) given the state estimates at the previous time step and are given by

$$\hat{\boldsymbol{x}}_{k|k-1} = \begin{bmatrix} f_d\left(p_{k-1}, \hat{x}_{k-1|k-1}\right) \\ \hat{\zeta}_{k-1|k-1} \end{bmatrix} + G u_{k-1} \tag{25a}$$

$$\hat{d}_{k|k-1} = \hat{d}_{k-1|k-1} \tag{25b}$$

The covariance matrix $P_{k|k-1}$ of the prediction error of the augmented state $\boldsymbol{x}_{k|k-1}$ is given by

$$P_{k|k-1} = F_{k-1} P_{k-1|k-1} F_{k-1}^T + Q_{k-1} \tag{25c}$$

Next, in the update step, the prediction is adjusted according the measurement sample y_k. The innovation residual is the difference between the measurement sample and the prediction of the measured quantity, and is based on the output equation (24d).

The innovation residual z_k, its covariance matrix S_k and the *near-optimal* Kalman gain L_k are given by

$$z_k = y_k - H_k \hat{\boldsymbol{x}}_{k|k-1} - \delta \hat{d}_{k|k-1} \tag{25d}$$

$$S_k = R_k + H_k P_{k|k-1} H_k^T \tag{25e}$$

$$L_k = P_{k|k-1} H_k^T S_k^{-1} \tag{25f}$$

Finally, the updated estimate $\hat{\boldsymbol{x}}_{k|k}$ of the augmented state, its covariance matrix $P_{k|k}$ and the estimated fringe jump state $\hat{d}_{k|k}$ are given by

$$\hat{\boldsymbol{x}}_{k|k} = \hat{\boldsymbol{x}}_{k|k-1} + L_k \left(z_k - \delta \mathbb{E}\left[\Delta_{k-1} \mid z_k \right] \right) \tag{25g}$$

$$\hat{d}_{k|k} = \hat{d}_{k|k-1} + \mathbb{E}\left[\Delta_{k-1} \mid z_k \right] \tag{25h}$$

$$P_{k|k} = \left(I - L_k H_k \right) P_{k|k-1} \tag{25i}$$

where $\mathbb{E}\left[\Delta_{k-1} \mid \tilde{z}_k \right]$ denotes the expected value of fringe jumps at time t_k given z_k, as discussed in the next subsection.

The EKF (25a)-(25i) iteratively produces estimates of the augmented state $\hat{\boldsymbol{x}}_{k|k}$, its associated covariance matrix $P_{k|k}$ and estimates of the fringe jump state $\hat{d}_{k|k}$, based on the measurements y_k, the inputs u_k and the initial values $\hat{\boldsymbol{x}}_{0|0}$ and $\hat{d}_{0|0} = 0$, where $k = 1, ..., N$. The computational speed of the EKF is dominated by (25a). Because the EKF uses a linearization of the nonlinear dynamics (24a) in (25c), the expressions for the matrices $P_{k|k-1}$ (25c), S_k (25e) and $P_{k|k}$ (25i) are approximations of the true covariance of the prediction error $\mathbb{E}\left[\left(\boldsymbol{x}_{k|k-1} - \hat{\boldsymbol{x}}_{k|k-1} \right) \left(\boldsymbol{x}_{k|k-1} - \hat{\boldsymbol{x}}_{k|k-1} \right)^T \right]$, the true covariance of the innovation residual $\mathbb{E}\left[z_k z_k^T \right]$ and the true covariance of the estimation error $\mathbb{E}\left[\left(\boldsymbol{x}_{k|k} - \hat{\boldsymbol{x}}_{k|k} \right) \left(\boldsymbol{x}_{k|k} - \hat{\boldsymbol{x}}_{k|k} \right)^T \right]$ respectively. No a priori guarantees can be given about the stability and estimation accuracy of the EKF and results have

to be checked a posteriori. Note also that the fringe jump state prediction $(25\,b)$ equals its estimate at the previous time step since we do not anticipate for fringe jumps. In Section 3.3, the estimation tradeoffs involved with choosing the covariance matrices Q_k^x, Q_k^ζ and R_k are discussed.

3.2. Fringe jump detection

Sensor errors can be detected from the innovation residual z_k, since it is the difference between measurements, containing the sensor errors, and the model-based prediction of the measured quantity.

Since fringe jumps have a magnitude of an integer multiple of δ on an interferometry channel, the c-th channel is flagged to contain a jump if both the magnitude of the innovation $|z_k^c|$ and its time difference $\left|z_k^c - z_{k-1}^c\right|$ exceed the thresholds $\gamma\delta$ and $\kappa\delta$ respectively, where z_k^c is the c-th element of the innovation z_k. Recall from Section 2.7 that $\delta = 2\pi c_{FIR}^{-1}$. The constants $\gamma \in (0,1)$ and $\kappa \in (0,1)$ set the detection sensitivity, where lower values of γ and κ increase the sensitivity, but also increase the false alarm probability. The expected value of fringe jumps at time t_k is composed of contributions of individual chords and is written as $\mathbb{E}\left[\Delta_{k-1} \mid \tilde{z}_k\right] = \mathbb{E}\left[\left[\Delta_{k-1}^1 \ldots \Delta_{k-1}^{n_{FIR}}\right]^T \mid z_k\right]$. The detected jump on chord c is denoted by $\mathbb{E}\left[\Delta_{k-1}^c \mid z_k\right]$ and is now chosen as

$$\mathbb{E}\left[\Delta_{k-1}^c \mid z_k\right] \approx \begin{cases} w\left(z_k^c\right) & \text{if } \left|z_k^c - z_{k-1}^c\right| \geq \kappa\delta \\ \\ 0 & \text{if } \left|z_k^c - z_{k-1}^c\right| < \kappa\delta \end{cases} \tag{26}$$

where the estimated jump magnitude $w\left(z_k^c\right)$ is chosen as a truncation function and is defined as $w\left(z_k^c\right) = \text{sgn}\left(z_k^c\right)\left\lceil\left|\frac{z_k^c}{\delta}\right| - \gamma\right\rceil$ where $\lceil a \rceil$ is the smallest integer larger then or equal to $a \in \mathbb{R}$. The corrected innovation residual is denoted by $\tilde{z}_k^c$ and is given by

$$\tilde{z}_k^c = z_k^c - \delta\,\mathbb{E}\left[\Delta_{k-1}^c \mid z_k^c\right] \tag{27}$$
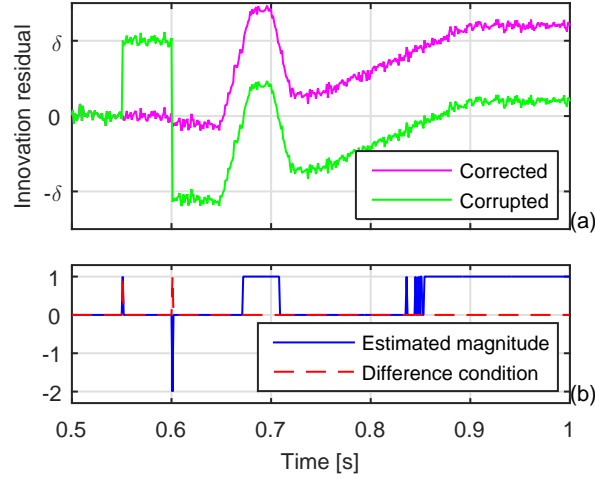
Figure 8. An example of an innovation signal z_k^c corrupted by a positive jump at $t = 0.55$s, a double negative jump at $t = 0.6$s and ramps/drifts between $t = 0.65$s and $t = 0.9$s is given in (a). The corrected innovation residual $\tilde{z}_k^c$ is also plotted. The estimated magnitude $w\left(z_k^c\right)$ and the time difference condition $\left|z_k^c - z_{k-1}^c\right| \geq \kappa\delta$ are shown in (b).

Observe that in (b), the jumps in the corrupted z_k^c exceed both the magnitude threshold and the ramp threshold. Consecutively, they are flagged as fringe jumps and are corrected for as desired. Note also in (b) that the ramps in z_k^c are correctly not flagged as fringe jumps since they do not exceed the time difference threshold even if they exceed the magnitude threshold.

Effectively, (27) is a modification of a wrapping, or modulo, operator applied on z_k^c.

It reduces to $\tilde{z}_k^c = z_k^c(\mathrm{mod}\ \delta)$ for $\gamma = 1$ and if $\left|z_k^c - z_{k-1}^c\right| \geq \kappa\delta$. We choose $\gamma = 0.9$

and $\kappa = 0.5$.

In this way, a jump on the c-th interferometry channel is flagged when both the

absolute value of the innovation $|z_k^c|$ exceeds the threshold $\gamma\delta$ and its time difference

$\left|z_k^c - z_{k-1}^c\right|$ exceeds the threshold $\kappa\delta$. The satisfactory response of the corrected

innovation $\tilde{z}_k^c$ to an example innovation signal z_k^c containing both jumps and ramps is

shown in Figure 8, including also the signals $w\left(z_k^c\right)$ and $\left|z_k^c - z_{k-1}^c\right| \geq \kappa\delta$.

The detected jump (26) is subtracted from the innovation residual in (27) (also

in (25g)) and stored in the fringe jump state $\hat{d}_k$ in (25h).

3.3. Design of the covariance matrices

The estimation accuracy and estimation convergence speed of an EKF is determined by the choice of the covariance matrices Q_k^x, Q_k^ζ and R_k (see e.g. [38]).

The measurement covariance matrix R_k is chosen a priori as the sample covariance of high-pass diagnostic data. The covariance is increased on distrusted output channels or channels whose numerical evaluation of the line-integrals are sensitive to errors in the equilibrium reconstruction, as discussed in Section 2.7. In this way, the EKF estimates rely less on interferometry chords deemed unreliable.

The choice of the covariance matrices Q_k^x and Q_k^ζ is a design tradeoff between estimation accuracy, estimation convergence speed and noise level of the estimated state. Furthermore, the choice of the spatial structure of Q_k^x and Q_k^ζ determines the smoothness of the estimated profiles and the spatial correlation of the disturbance estimates.

The process covariance matrix Q_k^x is chosen as a symmetric Toeplitz (constant-diagonal) matrix, with a descending first row. Its entries reflect the amount of uncertainty on the state evolution. Increasing the values of Q_k^x increases the Kalman gain L_k (see (25c) and (25f)) and thereby improves the estimation accuracy, but also increases the amplification of measurement noise to the state estimate. The values of the first row determine the spatial correlation of the estimated profile and are chosen as exponentially decaying values. Increasing the decay width causes the profile estimates to be more spatially correlated and thus smooth, but decreases the estimation convergence speed.

The disturbance covariance matrix Q_k^ζ is chosen as the product of a diagonal matrix Q_D and a symmetric Toeplitz matrix Q_T with a unit diagonal and a descending
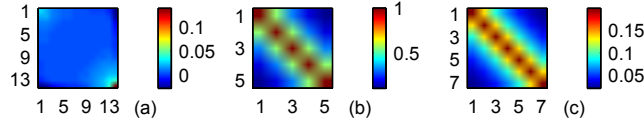
Figure 9. Graphical representation of the matrices R_k (a), Q^T (b) and Q_k^x (c).

first row. The entries of Q_D determine the rate at which the estimated state disturbances $\hat{\zeta}_k$ change. Increasing these increases the convergence speed of estimated model errors/disturbances. The values of the first row of Q_T determine the spatial correlation of the estimated disturbances and are chosen as exponentially decaying values. Increasing this decay width promotes smoothness of the estimated disturbances [39]. An example of the matrices R_k, Q^T and Q_k^x is given in Figure 9. In Section 3.4.1, the effects of two different settings is investigated.

3.4. Observer performance with simulated data

In this subsection, the estimation performance of the EKF on simulated data for TCV is assessed. The comparison allows to assess the estimation quality with respect to the simulated density. Results for two different settings of the Kalman gain (25*f*) and different numbers of interferometry chords are presented.

3.4.1. Estimation quality and tuning tradeoffs for different observer gains In order to assess the performance of the observer, two cases in which the observer estimates a *simulated* density profile with two different settings of the observer gain are shown. The system (16) is simulated and the observer (25*a*)-(26) is applied to the simulated diagnostic signals (22). Some model coefficients (see Table 1) used in the observer are perturbed with respect to those used in the simulation, representing inaccurate knowledge of the transport processes, to assess the ability of the observer to estimate

Table 1. Model perturbations

Coefficient	Unit	Nominal	Perturbed
D	$[\text{m}^2/\text{s}]$	1	0.8
ν	$[\text{m/s}]$	10	5
N_{sat}	$[\#]$	3×10^{19}	6×10^{19}
$\langle \sigma v \rangle_{\text{iz}} (T_{\text{e,b}})$	$[\text{m}^3/\text{s}]$	1×10^{-14}	2×10^{-14}

the density in the presence of modeling uncertainties. The simulation uses input and parameter data from TCV shot #41953 to recreate a realistic discharge scenario. White noise with the sample covariance of high-pass measurements of TCV shot #41953 is added to (22) as measurement noise.

The simulation results for the cases of high and low Kalman gain are shown in Figure 10 and Figure 11, respectively. As expected from the discussion in Section 3.3, a high Kalman gain yields accurate estimates of the density, as seen in the estimation error (Figure 10(c)), density profile (Figure 10(f)) and the spatial profile of the measurements (Figure 10(g)), but these estimates are affected by the measurement noise (Figure 10(c)(d)). On the other hand, a low Kalman gain yields less accurate estimates of the density, as seen in the estimation error (Figure 11(c)), density profiles (Figure 11(f)) and the spatial profile of the measurements (Figure 11(g)), but these estimates contain less measurement noise (Figure 11(c)(d)). However, in both cases the estimation error is favourably small and the disturbance estimate $\hat{d}_k$ compensates for systematic modeling errors formed by the perturbed coefficients.

While either choice for the Kalman gain used in this section has its advantages and drawbacks, optimal settings follow from requirements. We feel that an intermediate setting provides the best estimation accuracy and an acceptable noise level in the estimated density. In this case, we proceed with an intermediate gain with respect to the gains used in this section.
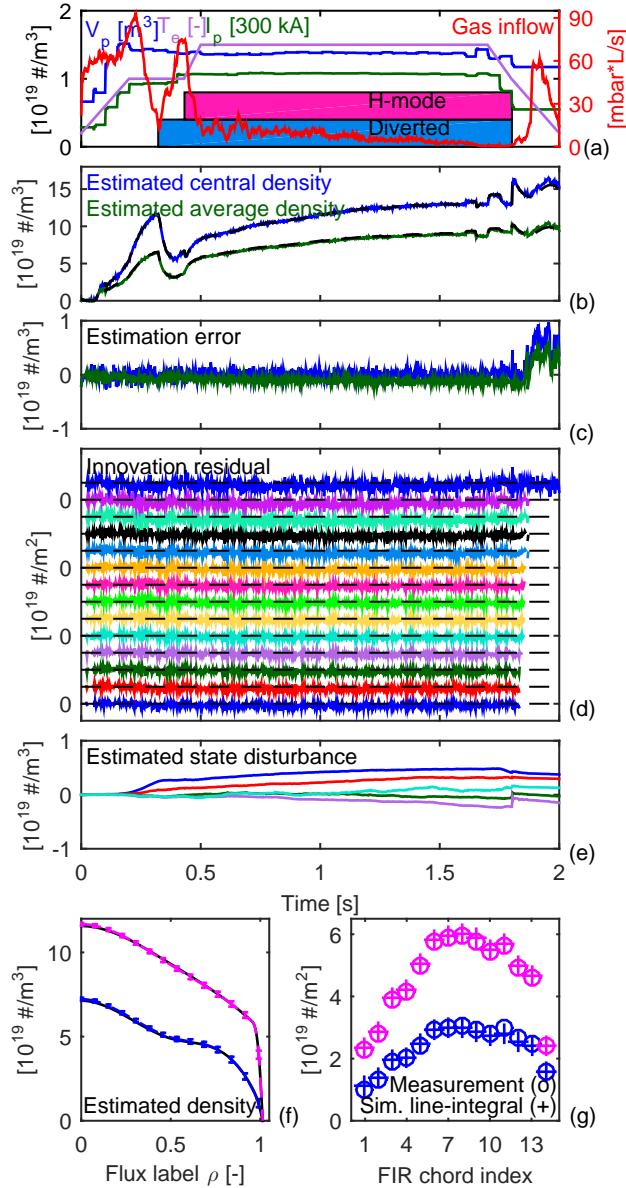
Figure 10. Observer results for simulated data. A high Kalman gain is used. The input and parameter data of TCV shot #41953 are shown in (a). The estimated central and average density are shown in (b), with simulated densities in black. The elements of the innovation residual (25*d*) are shown in (d), individually offset at intervals of $1 \times 10^{19}\,\mathrm{m}^{-2}$. The estimated disturbance is shown in (e). The estimated density profiles with confidence bounds at $t = 0.25$s (blue) and $t = 1$s (magenta) are shown in (f), with simulated profiles in black. The measurements and predicted measurements at these time slices are shown in (g).
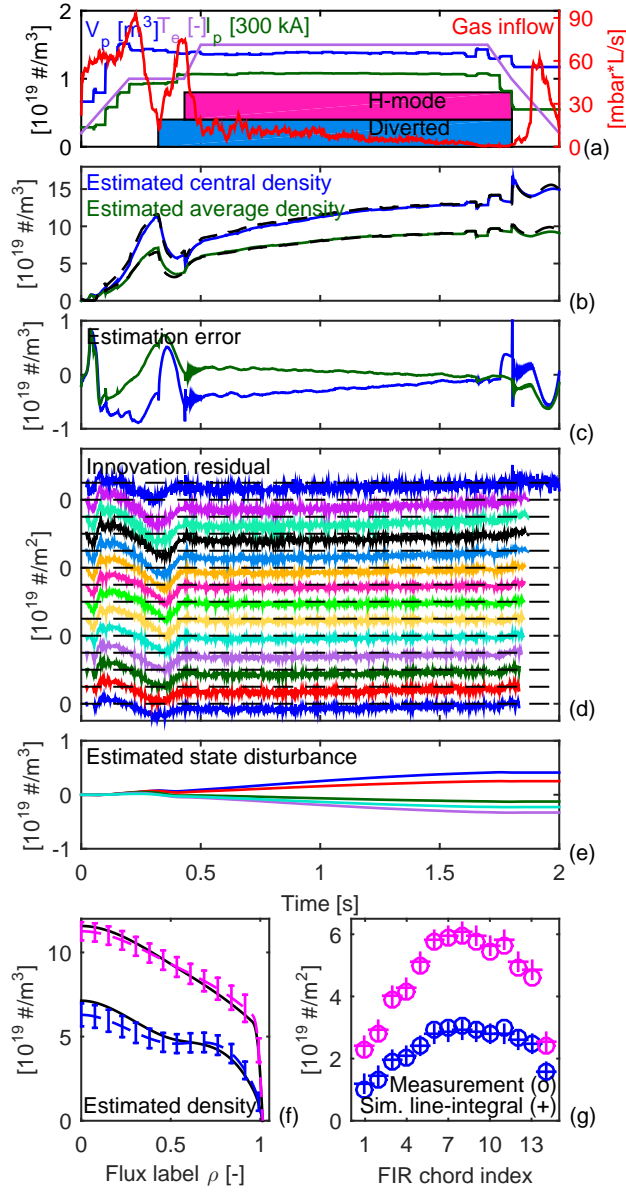
Figure 11. Observer results for simulated data. A low Kalman gain is used. The input and parameter data of TCV shot #41953 are shown in (a). The estimated central and average density are shown in (b), with simulated densities in black. The elements of the innovation residual (25*d*) are shown in (d), individually offset at intervals of $1 \times 10^{19}\,\mathrm{m}^{-2}$. The estimated disturbance is shown in (e). The estimated density profiles with confidence bounds at $t = 0.25$ (blue) and $t = 1$ (magenta) are shown in (f), with simulated profiles in black. The measurements and predicted measurements at these time slices are shown in (g).

3.4.2. Estimation quality for different numbers of interferometry channels The number of interferometry channels n_{FIR} is different for each tokamak. Existing density profile reconstruction methods require $m \leq n_{FIR}$ to invert $\Omega(p_k)$ in (22) and provide the static mapping $y_k \rightarrow \hat{x}_k$. The observer (25a)-(26) with $m = 5$ is applied on the system simulation from Section 3.4.1 for different subsets of the 14 interferometry channels of TCV. Again, the observer uses the perturbed coefficients with respect to those used in the simulation, see Table 1. In Figure 12, the observer performance is shown using either a central channel #7, a side channel #11, three channels #3,#7,#11, and all 14 channels. In case of using a single channel, the profile shape is entirely deduced from the model known to the observer. Consequently, the estimation error (see Figure 12(b)) is large and there are large differences between the simulated and estimated profile. While 14 output channels provide the best accuracy, only three channels already provide a small steady-state estimation error. This result can be attributed to the smoothness of the profile predicted by the model, while the update step keeps the predicted density evolution from drifting away from the measurements.

3.5. Observer performance with experimental data

In this section, the estimation performance of the observer on experimental data of TCV is assessed. While the true density profile is unknown, the innovation residual provides insight into the estimation performance of the observer.

3.5.1. Low density L-mode shot The performance of the observer on measurement data from TCV shot #47675 is shown in Figure 13. This shot contains two consecutive fringe jumps on chord #10. All 14 channels except three central and one outer
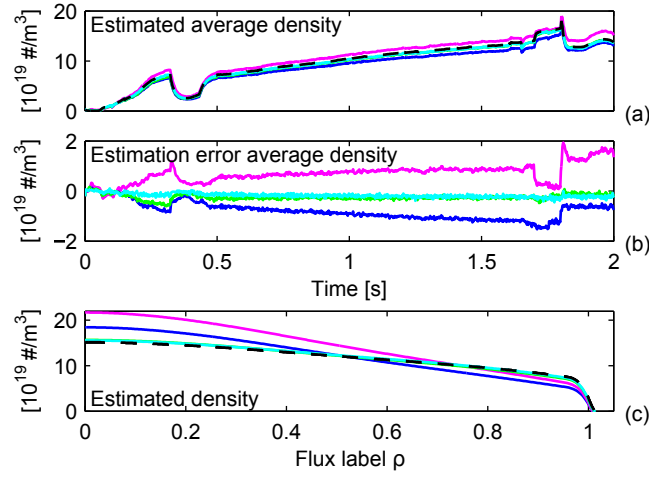
Figure 12. Observer response to different number of interferometry channels. The simulated density is shown as a black dashed line. Reconstructed densities using either central channel #7 (blue), side channel #11 (magenta), three channels #3,#7,#11 (green), all 14 channels (cyan). The density profiles at $t = 1$s are shown in the lower figure. In case of a single channel, the profile shape is deduced from the model. In case of multiple channels, the profile shape is reconstructed from the measurements. The reconstruction quality is best when all channels are used.

malfunctioning chords are used to estimate the density. The model coefficients used in the observer are those chosen in Section 2.10, which were found to be representative for a typical discharge in TCV. The values of the innovation residual are small (see Figure 13(c)(f)) in the first 0.5s of the discharge, implying a good estimation accuracy in this period. While two consecutive fringe jumps around $t = 0.33$s are correctly flagged and corrected (see Figure 13(f)), spatial discrepancies in the innovation residual around $t = 0.42$s and $t = 0.53$s (see Figure 13(c)(f)) exceed the detection threshold (26) and are therefore incorrectly flagged as jumps. We assign the latter to inaccurate evaluation of the line integrals (see Section 2.7) due to inaccurate information of $\psi(r, Z)$. On TCV, the interferometry chords are aligned vertically. Consequently, a small outward displacement of the plasma with respect to the reconstructed equilibrium can lead to larger values of the line-integrals on the

low-field side and lower values of the line-integrals at the high-field side. Moreover, the malfunction of three central chords implies that the central density must be extrapolated by the observer from the other chords using the model. Still, these false jump alerts and absence of central chords do not lead to unrealistic estimates of the density profile, as is seen in Figure 13(b)(e).

3.5.2. High density H-mode shot The performance of the observer on measurement data from TCV shot #47675 is shown in Figure 14. This shot contains no fringe jumps. All 14 channels except one malfunctioning chord are used to estimate the density. The values of the innovation residual are small (see Figure 14(c)(f)), implying a good estimation accuracy. However, high noise levels are seen in the estimated density in the middle section of the discharge caused by ELMs. As discussed in Section 3.3, there is a design tradeoff between estimation accuracy and noise in the estimates.

4. Future extensions and research

It is known that the fuelling efficiency of the gas valve with increasing electron temperature in the SOL as the ionization depth decreases [42, 67]. This is problematic for ITER and different actuators must be used instead for density control at high plasma temperature. Pellet injection is foreseen to provide fuelling at high temperature, while the strike point positions could influence the pumping and ECRH influences the peaking of the density profile. In the future we will extend the modeled ionization (6) with a temperature-dependent ionization distribution. This will allow the design of controllers which are able to deal with the changing fuelling efficiency of available actuators. Moreover we may model the effect of the strike point locations on pumping, and the pump-out mechanism: the influence of ECRH on the density
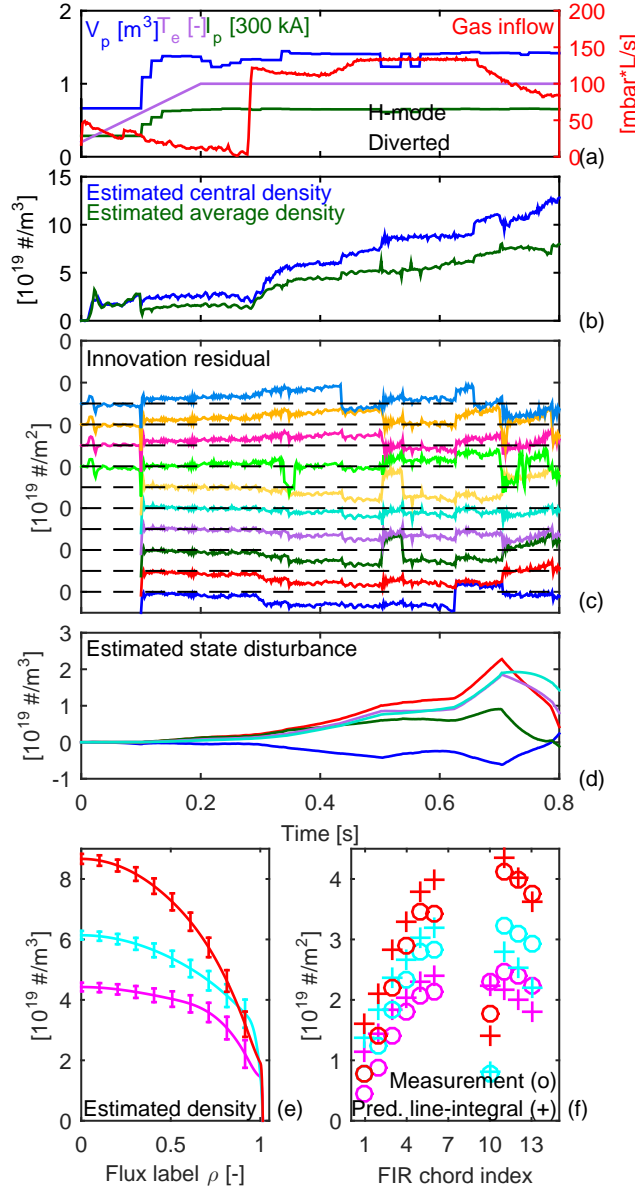
Figure 13. Observer results for experimental data of TCV shot #47675. The input and parameter data of this shot are shown in (a). The estimated central and average are shown in (b). The elements of the innovation residual ($25d$) are shown in (c), individually offset at intervals of $1 \times 10^{19}\,\mathrm{m^{-2}}$. The estimated disturbance is shown in (d). The estimated density profiles with confidence bounds at $t = 0.33$s (magenta), $t = 0.4$s (light blue) and $t = 0.6$s (red) are shown in (e). The measurements and predicted measurements at these time slices are shown in (f).
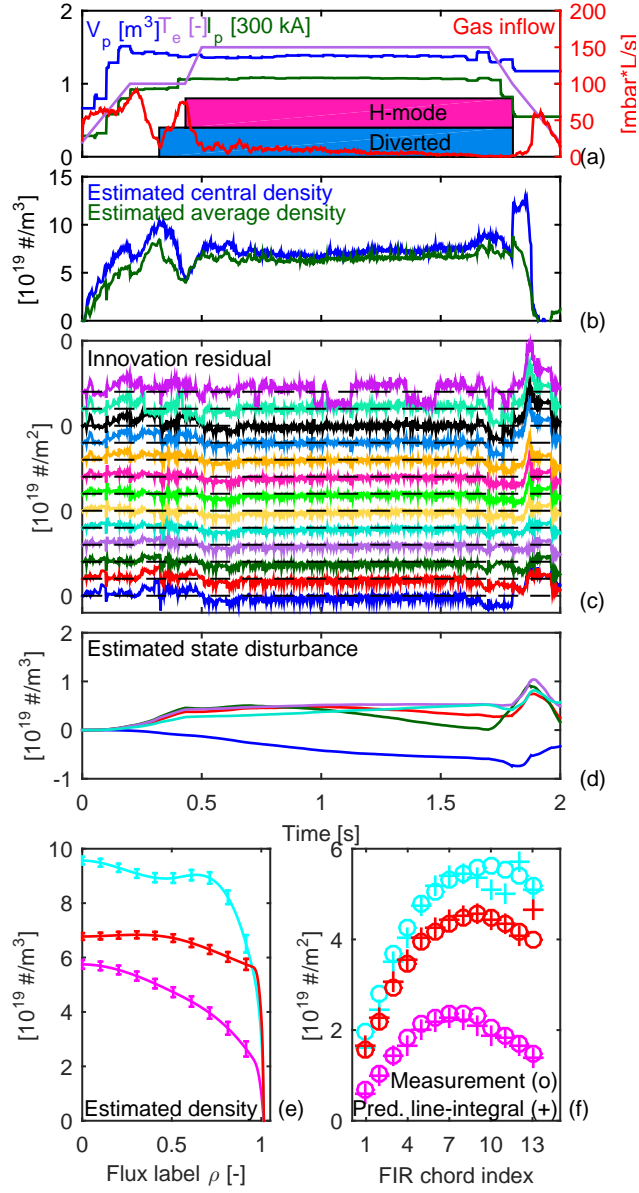
Figure 14. Observer results for experimental data of TCV shot #41953. The input and parameter data of this shot are shown in (a). The estimated central and average are shown in (b). The elements of the innovation residual $(25d)$ are shown in (c), individually offset at intervals of $1 \times 10^{19}\,\mathrm{m}^{-2}$. The estimated disturbance is shown in (d). The estimated density profiles with confidence bounds at $t = 0.12\mathrm{s}$ (magenta), $t = 0.3\mathrm{s}$ (light blue) and $t = 1\mathrm{s}$ (red) are shown in (e). The measurements and predicted measurements at these time slices are shown in (f).

transport.

Additional diagnostics systems such as Thomson scattering, Bremsstrahlung, reflectometry and polarimetry may be incorporated in the observer for even more reliable real-time density profile estimation. The detection of fringe jumps may be improved by incorporating the measurement residuals of neighbouring interferometry chords, or including information from other diagnostics.

The observer will be implemented on tokamak control systems in the near future, and tested against more detailed physics codes for ITER.

5. Conclusion

A model-based approach to the design of a real-time plasma density profile reconstruction algorithm has been presented.

A control-oriented model was derived from a spatially discretized plasma transport equation which takes main particle transport channels into account. Simulation results show that the model is able to reproduce the evolution of interferometry signals during a TCV and an ASDEX-Upgrade discharge with gas fuelling, by tuning the appropriate coefficients.

Based on this model, an extended Kalman filter was designed that estimates the density profile, state disturbances as well as fringe jumps in the interferometry signals. The state disturbance estimates form an effective way to compensate for model-reality mismatches, even with significant mismatch between the model assumed in the algorithm and the model used to simulate the system. Reconstructions on simulated data as well as offline reconstruction simulations on experimental data show that the observer estimates the density profile with a high accuracy. The accuracy increases with the number of measurement channels used and increases with a well-chosen

observer gain. The extensions mentioned in Chapter 4 as well as implementation, testing and validation on tokamak control systems are planned for the near future.

Acknowledgments

Appendix A. Numerical implementation

This appendix will treat the details of the numerical implementation, including the spatial and temporal discretization of the radial particle density transport equation (2) as well as some measures which have been taken to render the problem computationally efficient for real-time applications. Appendix A.1 treats the spatial discretization of the PDE using finite elements and Appendix A.2 shows the time discretization. Finally, Appendix A.3 shows how the line-integrals of the electron density in (20) are efficiently evaluated.

Appendix A.1. Spatial discretization using a finite-element method

The infinite-dimensional problem of the PDE (2) in the spatial coordinate ρ is transformed into a finite-dimensional problem using the finite-element method (see, e.g. [54]) similar to [55]. An important advantage of using a finite element method is that it allows efficient computation of the dynamics, required for real-time applications, and also that the order of spatial derivatives of the elements involved are, as we will see, one order lower than the order of the PDE.

The resulting system of ODEs will contain the physical quantities in the parameter

$$p(t) = \begin{bmatrix} c_{\mathrm{D}} & c_{\mathrm{H}} & T_{\mathrm{e,b}} & I_{\mathrm{p}} & V' & G_1 & G_0 & \Omega \end{bmatrix}$$ defined in Section 2.5, which lies in the parameter space $\mathcal{P}$, i.e. $p(t) \in \mathcal{P}$. For reasons of brevity, the parameter space is not explicitly specified, but the letter $\mathcal{P}$ is used to indicate functional dependencies of the parameter $p(t)$ in the remainder of this paper.

Consider our time-varying, inhomogeneous PDE (2) on the domain $\Omega = \{(t, \rho) \in \mathbb{R} \mid t_0 \leq t \leq t_{\mathrm{f}}, \, 0 \leq \rho \leq \rho_{\mathrm{e}}\}$

$$\frac{1}{V'} \frac{\partial}{\partial t} (n_e V') + \frac{1}{V'} \frac{\partial \Gamma}{\partial \rho} = S \tag{A.1}$$

with the radial particle flux Γ given by (3) and the net electron source S given by (4).

First, we approximate the electron density by

$$n_e(\rho, t) = \sum_{\alpha=1}^{m} \Lambda_\alpha(\rho) b_\alpha(t) \tag{A.2}$$

where the basis functions $\Lambda_\alpha : [0, \rho_{\mathrm{e}}] \to [0, 1]$, $\alpha = 1, ..., m$ are chosen as cubic B-splines with a finite support [56]. The knot sequence is denoted by $\rho_1 < \rho_2 < \cdots < \rho_{m-1} < \rho_m$ and we fix $\rho_1 = 0$, $\rho_{m-1} = 1$ and $\rho_m = \rho_{\mathrm{e}}$. The boundary conditions $\frac{\partial n_e}{\partial \rho}\big|_{\rho=0} = 0$ and $n_e|_{\rho=\rho_{\mathrm{e}}} = 0$ of Section 2.1.3 are satisfied by choosing the basis functions Λ_α as the appropriate linear combination of the B-splines [56] such that $\frac{\partial \Lambda_\alpha}{\partial \rho}\big|_{\rho=0} = 0$ and $\Lambda_\alpha(\rho_{\mathrm{e}}) = 0$ for every $\alpha = 1, ..., m$. For the purpose of control-

oriented modeling, a small number of density states $(m = 5)$ with closely-spaced knots near the plasma edge is chosen, see Figure 4 for an example of basis functions.

By substituting the electron density parameterization (A.2) in (A.1), (3) and (4), the electron density continuity is written as

$$\sum_{\alpha=1}^{m} \Lambda_\alpha \frac{\partial}{\partial t}(b_\alpha V') = \sum_{\alpha=1}^{m} b_\alpha \frac{\partial}{\partial \rho}\left(V'\left(G_1 D \frac{\partial \Lambda_\alpha}{\partial \rho} + G_0 \nu \Lambda_\alpha\right)\right)$$
$$+ V'S \qquad (A.3)$$

where the net electron source S is written as

$$S = \left(\Lambda_{\mathrm{iz}} \langle \sigma v \rangle_{\mathrm{iz}} (T_{\mathrm{e,b}}) \frac{N_{\mathrm{v}}}{V_{\mathrm{v}}} - \frac{H(\rho-1)}{\tau_{\mathrm{SOL}}}\right) \sum_{\alpha=1}^{m} b_\alpha \Lambda_\alpha$$
$$- \Lambda_{\mathrm{rec}} \langle \sigma v \rangle_{\mathrm{rec}} (T_{\mathrm{e,b}}) \left(\sum_{\alpha=1}^{m} b_\alpha \Lambda_\alpha\right)^2$$
$$+ \Lambda_{\mathrm{NBI}}\Gamma_{\mathrm{NBI}} + \Lambda_{\mathrm{pellet}}\Gamma_{\mathrm{pellet}} \qquad (A.4)$$

Projecting (A.3) onto a set of test functions $\Psi_\beta : [0, \rho_{\mathrm{e}}] \to [0, 1]$, $\beta = 1, ..., m$ and integrating over the spatial domain yields the weak formulation of (A.1). The test functions $\Psi_\beta(\rho)$, $\beta = 1, ..., m$ with $\sum_{\beta=1}^{m} \Psi_\beta(\rho) = 1$ are chosen as cubic B-splines with a finite support on the same knot sequence $\rho_1 < \cdots < \rho_m$. The weak form can be formulated for every $\beta = 1, 2, ..., m$ and is written as

$$\sum_{\alpha=1}^{m} \frac{db_\alpha}{dt} \int_0^{\rho_{\mathrm{e}}} \Psi_\beta \Lambda_\alpha V' d\rho = -\sum_{\alpha=1}^{m} b_\alpha \int_0^{\rho_{\mathrm{e}}} \frac{\partial V'}{\partial t} \Psi_\beta \Lambda_\alpha d\rho$$
$$+\sum_{\alpha=1}^{m} b_\alpha \int_0^{\rho_{\mathrm{e}}} \Psi_\beta \frac{\partial}{\partial \rho}\left(V'\left(G_1 D \frac{d\Lambda_\alpha}{d\rho} + G_0 \nu \Lambda_\alpha\right)\right) d\rho$$
$$+\int_0^{\rho_{\mathrm{e}}} \Psi_\beta S V' d\rho$$
$$= -\sum_{\alpha=1}^{m} b_\alpha \int_0^{\rho_{\mathrm{e}}} \frac{\partial V'}{\partial t} \Psi_\beta \Lambda_\alpha d\rho$$
$$-\sum_{\alpha=1}^{m} b_\alpha \int_0^{\rho_{\mathrm{e}}} \frac{d\Psi_\beta}{d\rho} V'\left(G_1 D \frac{d\Lambda_\alpha}{d\rho} + G_0 \nu \Lambda_\alpha\right) d\rho$$

$$+ \sum_{\alpha=1}^{m} b_\alpha \Psi_\beta V' \left(G_1 D \frac{d\Lambda_\alpha}{d\rho} + G_0 \nu \Lambda_\alpha \right) \Big|_0^{\rho_e}$$

$$+ \int_0^{\rho_e} \Psi_\beta S V' d\rho \tag{A.5}$$

Note that integration by parts is used which reduces the order of the maximum radial

derivative to be evaluated. The weak form is now written‡ as

$$\sum_{\alpha=1}^{m} [M]_{\beta\alpha} \frac{db_\alpha}{dt} = \sum_{\alpha=1}^{m} [H]_{\beta\alpha} b_\alpha + N_v \sum_{\alpha=1}^{m} [J]_{\beta\alpha} b_\alpha$$

$$+ \sum_{i=1}^{m} \sum_{\alpha=1}^{m} [L_\beta]_{i\alpha} b_\alpha b_i + [P]_\beta \begin{bmatrix} \Gamma_{\text{NBI}} \\ \\ \Gamma_{\text{pellet}} \end{bmatrix}$$

which can also be written in vector form

$$M \frac{db}{dt} = Hb + N_v Jb + \begin{bmatrix} b^T L_1 \\ \vdots \\ b^T L_m \end{bmatrix} b + P \begin{bmatrix} \Gamma_{\text{NBI}} \\ \\ \Gamma_{\text{pellet}} \end{bmatrix} \tag{A.6}$$

where the elements of the matrices functions $M, H, J, L_\beta : \mathcal{P} \to \mathbb{R}^{m \times m}$, $\beta = 1, ..., m$

and $P : \mathcal{P} \to \mathbb{R}^{m \times 2}$ are defined as

$$[M]_{\beta\alpha} = \int_0^{\rho_e} \Psi_\beta \Lambda_\alpha V' d\rho \tag{A.7}$$

$$[H]_{\beta\alpha} = -\int_0^{\rho_e} \frac{\partial V'}{\partial t} \Psi_\beta \Lambda_\alpha d\rho$$

$$- \int_0^{\rho_e} \frac{d\Psi_\beta}{d\rho} V' \left(G_1 D \frac{d\Lambda_\alpha}{d\rho} + G_0 \nu \Lambda_\alpha \right) d\rho$$

$$+ \Psi_\beta V' \left(G_1 D \frac{d\Lambda_\alpha}{d\rho} + G_0 \nu \Lambda_\alpha \right) \Big|_0^{\rho_e}$$

$$- \frac{1}{\tau_{\text{SOL}}} \int_1^{\rho_e} \Psi_\beta \Lambda_\alpha V' d\rho \tag{A.8}$$

$$[J]_{\beta\alpha} = \frac{\langle \sigma v \rangle_{\text{iz}}(T_{e,b})}{V_v} \int_0^{\rho_e} \Lambda_{\text{iz}} \Psi_\beta \Lambda_\alpha V' d\rho \tag{A.9}$$

$$[L_\beta]_{i\alpha} = - \langle \sigma v \rangle_{\text{rec}}(T_{e,b}) \int_0^{\rho_e} \Lambda_{\text{rec}} \Psi_\beta \Lambda_\alpha \Lambda_i V' d\rho \tag{A.10}$$

‡ For ease of notation, the i, j-th element of a matrix $A \in \mathbb{R}^{m \times n}$ or a matrix function $A : \mathcal{U} \to \mathbb{R}^{m \times n}$ is denoted as $[A]_{ij}$, where $i \in \{1, ..., m\}$, $j \in \{1, ..., n\}$ and $\mathcal{U}$ is the argument space.

$$[P]_\beta \quad = \int_0^{\rho_e} \Psi_\beta \left[\begin{array}{cc} \Lambda_{\mathrm{NBI}} & \Lambda_{\mathrm{pellet}} \end{array} \right] V' d\rho \tag{A.11}$$

The term $\Psi_\beta V' \left(G_1 D \frac{d\Lambda_\alpha}{d\rho} + G_0 \nu \Lambda_\alpha \right)\Big|_0^{\rho_e}$ in (A.8) reduces to $\Psi_\beta V' \left(G_1 D \frac{d\Lambda_\alpha}{d\rho} + G_0 \nu \Lambda_\alpha \right)\Big|_{\rho_e}$

since $V'|_{\rho=0} = 0$. This resulting term represents particle flux Γ at the domain bound-

ary ρ_e in the weak formulation (A.6). Therefore $\Gamma|_{\rho_e}$ has been added as an inflow to

the vacuum inventory (11). Note the nonlinear terms in (A.6).

Next, the wall and vacuum particle inventory balances (9) and (11) are written

as

$$\frac{dN_{\mathrm{w}}}{dt} = A_{\mathrm{wb}} b + A_{\mathrm{ww}} N_{\mathrm{w}} + A_{\mathrm{wv}} N_{\mathrm{v}} + A_2 N_{\mathrm{w}} b \tag{A.12}$$

$$\frac{dN_{\mathrm{v}}}{dt} = A_{\mathrm{vb}} b + A_{\mathrm{vw}} N_{\mathrm{w}} + A_{\mathrm{vv}} N_{\mathrm{v}} - A_2 N_{\mathrm{w}} b$$

$$+ A_{\mathrm{iz}} N_{\mathrm{v}} b + b^T A_{\mathrm{rec}} b + \Gamma_{\mathrm{valve}} \tag{A.13}$$

where the elements of the row functions $A_{\mathrm{wb}}, A_2, A_{\mathrm{vb}}, A_{\mathrm{iz}} : \mathcal{P} \to \mathbb{R}^{1 \times m}$, the elements

of the matrix function $A_{\mathrm{rec}} : \mathcal{P} \to \mathbb{R}^{m \times m}$, the functions $A_{\mathrm{wv}}, A_{\mathrm{vv}} : \mathcal{P} \to \mathbb{R}$ and the

constants $A_{\mathrm{ww}}, A_{\mathrm{vw}} \in \mathbb{R}$ are defined as

$$[A_{\mathrm{wb}}]_\alpha \quad = \frac{1}{\tau_{\mathrm{SOL}}} \int_1^{\rho_e} \Lambda_\alpha V' d\rho \tag{A.14}$$

$$A_{\mathrm{ww}} \quad = - \tau_{\mathrm{release}}^{-1} \qquad A_{\mathrm{vw}} = -A_{\mathrm{ww}}$$

$$A_{\mathrm{wv}} \quad = \frac{c_{wv} V_{\mathrm{v},0}}{V_{\mathrm{v}} \tau_{\mathrm{release}}} \qquad A_{\mathrm{vv}} = -A_{\mathrm{wv}} - \frac{V_{\mathrm{v},0}}{V_{\mathrm{v}} \tau_{\mathrm{pump}}}$$

$$A_2 \quad = - N_{\mathrm{sat}}^{-1} A_{\mathrm{wb}}$$

$$[A_{\mathrm{vb}}]_\alpha \quad = - V' \left(G_1 D \frac{d\Lambda_\alpha}{d\rho} + G_0 \nu \Lambda_\alpha \right)\Big|_{\rho_e}$$

$$[A_{\mathrm{iz}}]_\alpha \quad = - \frac{\langle \sigma v \rangle_{\mathrm{iz}} (T_{\mathrm{e,b}})}{V_{\mathrm{v}}} \int_0^{\rho_e} \Lambda_{\mathrm{iz}} \Lambda_\alpha V' d\rho \tag{A.15}$$

$$[A_{\mathrm{rec}}]_{i\alpha} = n_e \langle \sigma v \rangle_{\mathrm{rec}} (T_{\mathrm{e,b}}) \int_0^{\rho_e} \Lambda_{\mathrm{rec}} \Lambda_i \Lambda_\alpha V' d\rho \tag{A.16}$$

Finally, (A.6) is premultiplied by M^{-1} and stacked with (A.12)-(A.13) to get the

nonlinear system of ODEs

$$\frac{dx}{dt} = A(p(t))\, x(t) + f(p(t), x(t)) + Bu(t) \tag{A.17}$$

where state vector $x(t) \in \mathbb{R}^{n_x}$ with $n_x = m + 2$ and the input vector $u(t) \in \mathbb{R}^{n_u}$ with

$n_u = 3$ are defined as

$$x(t) = \begin{bmatrix} b(t) \\ N_{\text{w}}(t) \\ N_{\text{v}}(t) \end{bmatrix} \qquad u(t) = \begin{bmatrix} \Gamma_{\text{valve}}(t) \\ \Gamma_{\text{NBI}}(t) \\ \Gamma_{\text{pellet}}(t) \end{bmatrix}$$

The matrix function $A : \mathcal{P} \to \mathbb{R}^{n_x \times n_x}$, the vector function $f : \mathcal{P} \times \mathbb{R}^{n_x} \to \mathbb{R}^{n_x}$ and

the matrix $B \in \mathbb{R}^{n_x \times n_u}$ are defined as

$$A(p) = \begin{bmatrix} M^{-1}H & 0 & 0 \\ A_{\text{wb}} & A_{\text{ww}} & A_{\text{wv}} \\ A_{\text{vb}} & A_{\text{vw}} & A_{\text{vv}} \end{bmatrix} \tag{A.18}$$

$$f(p, x) = \begin{bmatrix} M^{-1}JN_{\text{v}}b + M^{-1} \begin{bmatrix} b^T L_1 \\ \vdots \\ b^T L_m \end{bmatrix} b \\ A_2 N_{\text{w}} b \\ -A_2 N_{\text{w}} b + A_{\text{iz}} N_{\text{v}} b + b^T A_{\text{rec}} b \end{bmatrix} \tag{A.19}$$

$$B = \begin{bmatrix} 0 & M^{-1}P \\ 0 & 0 \\ 1 & 0 \end{bmatrix} \tag{A.20}$$

To quickly compute (A.18)-(A.20), the integrals in (A.7)-(A.11) and (A.14)-(A.16)
can be precomputed if the integrands do not depend on time, i.e. if all time- and space-
dependent variables are written as (a sum of) products of time-varying variables and
functions of ρ. This was naturally done for the electron density in (A.2) but is also

done for ν, V' and the mode-dependent D, ν_0, N_{sat}, τ_{SOL}, Λ_{iz}. The time-varying part of V' is separated as e.g. $V' = \frac{\partial V}{\partial \rho} \approx 2\rho V_{\text{p}}(t)$. For example, (A.7) is written as a product $M = 2V_{\text{p}}(t) Z_{\text{M}}$ where the matrix $Z_{\text{M}} \in \mathbb{R}^{m \times m}$ does not depend on time and is given by

$$[Z_{\text{M}}]_{\beta\alpha} = \int_0^{\rho_{\text{e}}} \rho \Psi_\beta \Lambda_\alpha d\rho$$

Next, this integral and (A.8)-(A.11) and (A.14)-(A.16) are numerically evaluated using Legendre-Gauss quadrature [68] as is also done in [40], for each combination of the switching parameters $c_{\text{D}} \times c_{\text{H}} \in \{0, 1\} \times \{0, 1\}$.

Appendix A.2. Time discretization using a trapezoidal method

The system of continuous-time ODEs (A.17) can be discretized in time. Consider an equidistant time grid $t_k = t_0 + kT_{\text{s}}$, $k \in \{0, 1, ..., N\}$ where $T_{\text{s}} > 0$ is the time step and $N = (t_{\text{f}} - t_0)/T_{\text{s}} \in \mathbb{N}$. We choose a finite difference approximation of the time derivative $\frac{dx}{dt}\big|_{t_k} \approx (x_{k+1} - x_k)/T_{\text{s}}$ and apply the trapezoidal method on (A.17) to get

$$\frac{x_{k+1} - x_k}{T_{\text{s}}} = (1 - \theta)\left(A\left(p_k\right) x_k + f\left(p_k, x_k\right) + Bu_k\right)$$
$$+ \theta\left(A\left(p_{k+1}\right) x_{k+1} + f\left(p_{k+1}, x_{k+1}\right)\right)$$
$$+ Bu_{k+1}) \tag{A.21}$$

where the discrete-time state, input and parameter are defined as $x_k = x(t_k)$, $u_k = u(t_k)$ and $p_k = p(t_k)$ respectively, and $\theta \in [0, 1]$ is a discretization parameter§. We choose $\theta = \frac{1}{2}$. For practical reasons, the approximations $p_{k+1} \approx p_k$ and $u_{k+1} \approx u_k$ are applied. To obtain a stable scheme that requires no iterations, we set $f\left(p_{k+1}, x_{k+1}\right) \approx f\left(p_k, x_k\right)$.

§ This is a generalization of the trapezoidal rule; $\theta = \frac{1}{2}$ yields the trapezoidal rule, whereas $\theta = 0$ and $\theta = 1$ yield the forward and backward Euler method respectively.

Rewriting (A.21) and applying these approximations yields the nonlinear system of difference equations

$$x_k = f_{\mathrm{d}}\left(p_{k-1}, x_{k-1}\right) + B_{\mathrm{d}}\left(p_{k-1}\right) u_{k-1} \tag{A.22}$$

where $f_{\mathrm{d}} : \mathcal{P} \times \mathbb{R}^{n_x} \to \mathbb{R}^{n_x}$ and $B_{\mathrm{d}} : \mathcal{P} \to \mathbb{R}^{n_x \times n_u}$ are defined as

$$f_{\mathrm{d}}\left(p_k, x_k\right) = \left(I - \theta T_{\mathrm{s}} A\left(p_k\right)\right)^{-1} \left[(1 - \theta) T_{\mathrm{s}} A\left(p_k\right) x_k\right.$$

$$\left. + T_{\mathrm{s}} f\left(p_k, x_k\right)\right]$$

$$B_{\mathrm{d}}\left(p_k\right) = \left(I - \theta T_{\mathrm{s}} A\left(p_k\right)\right)^{-1} T_{\mathrm{s}} B$$

Appendix A.3. Numerical evaluation of line integrals

The spatial discretization (A.2) and an equilibrium $\psi\left(R, Z\right)$ allow to write the line integrals in the measurement equation (22) as a linear combination of the state x_k. The output equation (22) is given by

$$y_k = C\left(p_k\right) x_k + \delta d_k$$

where $C\left(p_k\right) = \begin{bmatrix} \Omega\left(p_k\right) & 0^{n_{FIR} \times 2} \end{bmatrix}$ and the matrix function $\Omega : \mathcal{P} \to \mathbb{R}^{n_{FIR} \times m}$ is defined as

$$[\Omega]_{i\alpha} = \int_{L_i} \Lambda_\alpha\left(\rho\left(r, Z\right)\right) dL \tag{A.23}$$

First, the spatial distribution of ψ is assumed to be available from real-time 2D equilibrium reconstruction on a rectangular R-Z grid of the plasma cross-section (see e.g. [51, 53]). It is assumed that $\rho\left(\psi\right)$ is known.

Next, the integrals are divided in intervals of subsequent points $X_p^{(i)} = [R_p^{(i)} \; Z_p^{(i)}]^T$, $p = 1, ..., n_{\mathrm{p}}$ which are defined as the intersections between the i-th chord and the rectangular grid lines.

$$[\Omega]_{i\alpha} = \sum_{p=1}^{n_{\mathrm{p}}-1} \int_{X_p^{(i)}}^{X_{p+1}^{(i)}} \Lambda_\alpha\left(\rho\left(X\right)\right) dL$$

Finally, the integrals in (A.23) are numerically evaluated using the trapezoidal method as

$$[\Omega]_{i\alpha} \approx \sum_{p=1}^{n_{\mathrm{p}}-1} \frac{\Lambda_\alpha \left(\rho \left(X_{p+1}^{(i)} \right) \right) + \Lambda_\alpha \left(\rho \left(X_p^{(i)} \right) \right)}{2} L_p^{(i)}$$

where $\Lambda_\alpha \left(\rho \left(X_p^{(i)} \right) \right)$ is approximated by a linear interpolation between the function values $\Lambda_\alpha \left(\rho \left(X \right) \right)$ evaluated at the two R-Z grid points adjacent to the chord-grid intersection point $X_p^{(i)}$, and $L_p^{(i)} = \sqrt{\left(X_{p+1}^{(i)} \right)^2 + \left(X_p^{(i)} \right)^2}$, $p = 1, ..., n_{\mathrm{p}} - 1$ is the distance between subsequent chord-grid intersection points.

References

[1] Pironti A and Walker M 2005 *Control Systems, IEEE* **25** 24 – 29

[2] Moreau D, Walker M, JR F, Liu F, Schuster E, Barton J E, Boyer M D, Burrell K H, Flanagan S M, Gohil P, Groebner R, Holcomb C, Humphreys D, Hyatt A, JohnsoJohnson R D, La Haye R J, Lohr J, Luce T, Park J M, Penaflor B G, Shi W, Turco F, Wehner W, the ITPA-IOS group members and experts 2013 *Nuclear Fusion* **53** URL http://iopscience.iop.org/0029-5515/53/6/063020

[3] Boyer M D, Barton J E, Schuster E, Walker M L, C L T, JR F, Penaflor B G, Johnson R D and Humphreys D A 2014 *IEEE Transactions on Control Systems Technology* **22** URL http://ieeexplore.ieee.org/xpl/articleDetails.jsp?arnumber=6731565

[4] Barton J E, Boyer M D, Shi W, Schuster E, Luce T C, Ferron J R, Walker M L, Humphreys D A, Penaflor B G and Johnson R D 2012 *Nuclear Fusion* **52** 123018 URL http://stacks.iop.org/0029-5515/52/i=12/a=123018

[5] Maljaars E, Felici F, de Baar M, van Dongen J, Hogeweij G, Geelen P and Steinbuch M 2015 *Nuclear Fusion* **55** 023001 URL http://stacks.iop.org/0029-5515/55/i=2/a=023001

[6] Wesson J A 2004 *Tokamaks* 3rd ed (Oxford University Press)

[7] Boozer A 2012 *Physics of Plasmas* **19**

[8] Zohm H 2014 *Magnetohydrodynamic Stability of Tokamaks* (Wiley)

[9] Hender T, Wesley J, Bialek J, Bondeson A, Boozer A, Buttery R, Garofalo A, Goodman T, Granetz R, Gribov Y, Gruber O, Gryaznevich M, Giruzzi G, Gnter S, Hayashi N, Helander P, Hegna C, Howell D, Humphreys D, Huysmans G, Hyatt A, Isayama A, Jardin S, Kawano Y, Kellman A, Kessel C, Koslowski H, Haye R L, Lazzaro E, Liu Y, Lukash V, Manickam J, Medvedev S, Mertens V, Mirnov S, Nakamura Y, Navratil G, Okabayashi M, Ozeki T, Paccagnella R, Pautasso G, Porcelli F, Pustovitov V, Riccardo V, Sato M, Sauter O, Schaffer M, Shimada M, Sonato P, Strait E, Sugihara M, Takechi M, Turnbull A, Westerhof E, Whyte D, Yoshino R, Zohm H, the ITPA MHD D and Group M C T 2007 *Nuclear Fusion* **47** S128 URL http://stacks.iop.org/0029-5515/47/i=6/a=S03

[10] Loarte A, Lipschultz B, Kukushkin A, Matthews G, Stangeby P, Asakura N, Counsell G, Federici G, Kallenbach A, Krieger K, Mahdavi A, Philipps V, Reiter D, Roth J, Strachan J, Whyte D, Doerner R, Eich T, Fundamenski W, Herrmann A, Fenstermacher M, Ghendrih P, Groth M, Kirschner A, Konoshima S, LaBombard B, Lang P, Leonard A, Monier-Garbet P, Neu R, Pacher H, Pegourie B, Pitts R, Takamura S, Terry J, Tsitrone E, the ITPA Scrape-off Layer and Group D P T 2007 *Nuclear Fusion* **47** S203 URL http://stacks.iop.org/0029-5515/47/i=6/a=S04

[11] Gribov Y, Humphreys D, Kajiwara K, Lazarus E, Lister J, Ozeki T, Portone A, Shimada M, Sips A and Wesley J 2007 *Nuclear Fusion* **47** S385 URL http://stacks.iop.org/0029-5515/47/i=6/a=S08

[12] Biel W, de Baar M, Dinklage A, Felici F, Knig R, Meister H, Treutterer W and Wenninger R 2015 *Fusion Engineering and Design* **9697** 8 – 15 ISSN 0920-3796 proceedings of the 28th Symposium On Fusion Technology (SOFT-28) URL http://www.sciencedirect.com/science/article/pii/S0920379615000733

[13] Hutchinson I H 2005 *Principles of Plasma Diagnostics* (Cambridge University Press)

[14] Donné A J H 1995 *Review of Scientific Instruments* **66** 3407–3423

[15] Donné A J H, Barth C and Weisen H 2006 *Fusion Science and Technology* URL https://crppwww.epfl.ch/ weisen/publications/FSTchap4.pdf

[16] Weiwen X, Zetian L, Xuantong D, Zhongbing S and Zhuravlev V 2006 *Plasma Science and Technology* **8** 133 URL http://stacks.iop.org/1009-0630/8/i=2/a=02

[17] Mlynek A 2010 *Real-time control of the plasma density profile on ASDEX Upgrade* Ph.D. thesis Ludwig-Maximilians-Universität München

[18] Mlynek A, Reich M, Giannone L, Treutterer W, Behler K, Blank H, Buhler A, Cole R, Eixenberger H, Fischer R, Lohs A, Lddecke K, Merkel R, Neu G, Ryter F, Zasche D and the ASDEX Upgrade Team 2011 *Nuclear Fusion* **51** 043002 URL http://stacks.iop.org/0029-5515/51/i=4/a=043002

[19] Park H K 1989 *Plasma Physics and Controlled Fusion* **31** 2035

[20] Chiang K L, Hallock G A, Wootton A J and Wang L 1997 *Review of Scientific Instruments* **68** 894–897

[21] Koponen J P T and Dumbrajs O 1997 *Review of Scientific Instruments* **68** 4038–4042

[22] Furno I, Weisen H, Carey C, Angioni C, Behn R, Fable E, Zabolotsky A, the TCV team and contributors J 2005 *Plasma Physics and Controlled Fusion* **47** 49–69

[23] Fischer R and Dinklage A 2004 *Review of Scientific Instruments* **75**

[24] Fischer R, Wendland C, Dinklage A, Gori S, Dose V and the W7-AS team 2002 *Plasma Physics and Controlled Fusion* **44**

[25] Maddison G, Turner A, Fielding S and You S 2006 *Plasma Physics and Controlled Fusion* **48** 71–107

[26] Murari A, Zabeo L, Boboc A, Mazon D and Riva M 2006 *Review of Scientific Instruments* **77** 073505

[27] Zabeo L, Murari A, Innocente P, Joffrin E, Mazon D, Riva M and contributors J E 2004 *Review of Scientific Instruments*

[28] Gil C, Boboc A, Barbuti A, Pastor P and contributors J E 2010 *Journal of Physics: Conference Series* **227** 012032

[29] Hinton F and Hazeltine R 1976 *Review of Modern Physics* **48** 239–308

[30] Pereverzev G V and Yushmanov P N 2002 ASTRA. Automated System for TRansport Analysis in a tokamak Tech. Rep. 5/98 IPP Report

[31] Stangeby P 2000 *The plasma boundary of magnetic fusion devices* (Taylor & Francis Group)

[32] Fielding S, McCracken G and Stott P 1978 *Journal of Nuclear Materials* **76 & 77** 273–278

[33] Wong Y, Hallock G A, Rowan W L and Wootton A J 1992 *Journal of Nuclear Materials* **196-198** 1018–1021

[34] Vijvers W, Felici F, Le H, Duval B, Coda S and the TCV team 2012 Non-linear digital real-time control in the TCV tokamak *39th EPS Conference on Plasma Physics 2012 (EPS 2012) and the 16th International Congress on Plasma Physics*

[35] Brelen H E O 1994 *Fusion Technology* **27** 162–170

[36] Juhn J W, Hwang Y S, Hahn S H, Nam Y U, Yu Y W and Hong S H 2012 A global particle/balance model for wall interaction analysis associated with open- and closed/loop density control experiments in KSTAR *24th IAEA Fusion Energy Conference*

[37] Boncagni L, Pucci D, Piesco F, Zarfati E, Mazzitelli G and Monaco S 2013 *Fusion Engineering and Design* **88** 1097 – 1100 ISSN 0920-3796 proceedings of the 27th Symposium On Fusion Technology (SOFT-27); Lige, Belgium, September 24-28, 2012 URL http://www.sciencedirect.com/science/article/pii/S0920379613003190

[38] Anderson B D O and Moore J B 1979 *Optimal filtering* (Prentice-Hall, Inc.)

[39] Felici F, de Baar M and Steinbuch M 2014 A dynamic state observer for real-time reconstruction of the tokamak plasma profile state and disturbances *American Control Conference (ACC), 2014* pp 4816–4823

[40] Felici F 2011 *Real-time control of tokamak plasmas: from control of physics to physics-based control* Ph.D. thesis École Polytechnique Fédérale de Lausanne (EPFL) CH-1015 Lausanne, Switzerland

[41] Tamain P, Tsirone E, Ghendrih P, Gunn J, Clairet F, Bucalossi J and Pgouri B 2007 *Journal of Nuclear Materials* **363-365** 844–848

[42] Romanelli M, Parail V, da Silva Aresta Belo P, Corrigan G, Garzotti L, Harting D, Koechl F, Militello-Asp E, Ambrosino R, Cavinato M, Kukushkin A, Loarte A, Mattei M and Sartori R 2015 *Nuclear Fusion* **55**

[43] Artaud J, Basiuk V, Imbeaux F, Schneider M, Garcia J, Giruzzi G, Huynh P, Aniel T, Albajar F, An J, Bcoulet A, Bourdelle C, Casati A, Colas L, Decker J, Dumont R, Eriksson L, Garbet X, Guirlet R, Hertout P, Hoang G, Houlberg W, Huysmans G, Joffrin E, Kim S, Kchl F, Lister J, Litaudon X, Maget P, Masset R, Pgouri B, Peysson Y, Thomas P, Tsitrone E and Turco F 2010 *Nuclear Fusion* **50** 043001 URL http://stacks.iop.org/0029-5515/50/i=4/a=043001

[44] Zabolotsky A, Weisen H, Karpushov A, the TCV team and contributors J E 2006 *Nuclear Fusion* **46** 594–607

[45] Willensdorfer M, Fable E, Wolfrum E, Aho-Mantila L, Aumayr F, Fischer R, Reimold F, Ryter F and the ASDEX Upgrade team 2013 *Nuclear Fusion* **53**

[46] Pankin A, McCune D, Andre R, Bateman G and Kritz A 2004 *Journal of Computational Physics* **159** 157–184

[47] Feng Y, Wolle B and Hubner K 1995 *Computer Physics Communications* **88** 161–172

[48] Willensdorfer E, Wolfrum E, Scarabosio A, Aumayr F, Fischer R Kurzan B, McDermott R, Mlynek A, Nold B, Rathgeber S, Rohde V, Ryter F, Sauter P, Viezzer E and the ASDEX Upgrade team 2012 *Nuclear Fusion* **52**

[49] Rohde V, Mayer M, Mertens V, Neu R, Sugiyama K and the ASDEX team 2009 *Nuclear Fusion* **49**

[50] Rohde V, Kallenback A, Mertens V, Neu R and the ASDEX Upgrade team 2009 *Plasma Physics and Controlled Fusion* **51**

[51] Moret J M, Duval B P, Le H B, Coda S, Felici F and Reimerdes H 2015 *Fusion Engineering and Design* **91**

[52] Blum J, Boulbe C and Faugeras B 2012 *Journal of Computational Physics* **231**

[53] Ferron J R, Walker M L, Lao L L, St John H E, Humphreys D A and Leuer J A 1998 *Nuclear Fusion* **38.7** 1055

[54] Hughes T 1987 *The Finite Element Method* (Englewood Cliffs, NJ: Prentice Hall)

[55] Felici F and Sauter O 2012 *Plasma Physics and Controlled Fusion*

[56] de Boor C 2001 *A practical guide to splines* (*Applied Mathematical Science* vol 27) (Springer-Verlag)

[57] Weisen H, Dutch M J, Hofmann F, Martin Y, Moret J M, Nieswand C, Pietrzyk Z A, A P R and Pochelon A 1996 *Plasma Physics and Controlled Fusion* **38** 1415–1419

[58] Paley J, Coda S, Duval B P, Felici F, Moret J M and the TCV team 2010 Architecture and commissioning of the tcv distributed feedback control system *Real Time Conference, 17th IEEE-NPSS* (IEEE)

[59] Boboc A, Gelfusa M, Murari A, Gaudio P and contributors J E 2010 Recent developments of the jet far infrared interferometer-polarimeter diagnostic *Proceedings of the 18th High Temperature Plasma Diagnostics*

[60] Barry S 1999 *The extension of the FIR interferometer of TCV to a polarimeter and measurements of the Faraday rotation caused by the poloidal magnetic field* Ph.D. thesis University of Ireland, Cork

[61] Pochelon A, Goodman T, Henderson M, Angioni C, Behn R, Coda S, Hofmann F, Hogge J P, Kirneva N, Martynov A A, Moret J M, Pietrzyk Z A, Porcelli F, Reimerdes H, Rommers J, Rossi E, Sauter O, Tran M, Weisen H, Alberti S, S B, Blanchard P, Bosshard P, Chavan R, Duval B, Esipchuck Y V, Fasel D, Favre A, Franke S, Furno I, Gorgerat P, Isoz P F, Joye B, Lister J, Llobet X, Magnin J C, Mandrin P, Manini A, Marletaz B, Marmillod P, Martin Y, J-M M, Mlynar J, Nieswand C, Paris P, Perez A, Pitts R A, Razumova K, Refke A, Scavino E, Sushkov A, Tonetti G, Troyon F, Van Toledo W and Vyas P 1999 *Nuclear Fusion* **39**

[62] Weisen H, Moret J M, Franke S, Furno I, Martin Y, Anton M, Behn R, Dutch M J, Duval B P, Hofmann F, Joye B, Nieswand C, Pietrzyk Z A and Van Toledo W 1997 *Nuclear Fusion* **37** 1741–1758

[63] Kirneva N A, Behn R, Canal G P, Coda S, Duval B P, Goodman T P, Labit B, Mustafin N A, Karpushov A N, Pochelon A, Porte L, Sauter O, Silva M, Tal B and Vuille V 2015 *Plasma Physics and Controlled Fusion* **57** 025002 URL http://stacks.iop.org/0741-3335/57/i=2/a=025002

[64] Moreno V and Pigazo A (eds) 2009 *Kalman Filter Recent Advances and Applications* (InTech)

[65] Mechoud S, Witrant E, Dugard L and Moreau D 2013 Joint diffusivity and source estimation in tokamak heat transport *American Control Conference (ACC)* (Washington DC, United States: IEEE)

[66] Xu C, Ou Y and Schuster E 2010 *IEEE Transactions on Plasma Science* **38** 359 – 364 URL 10.1109/TPS.2009.2038220

[67] Belo P, Romanelli M, Parail V, Corrigan G, Harting D, Garzotti L, Koechl F, Militello-Asp E, Mattei M, Ambrosino R, Loarte A, Kukushkin A, Sartori R and Cavinato M 2015 Coupled core/sol modelling of fuelling requirements during the current ramp-up of iter l-mode plasmas *42nd EPS Conference on Plasma Physics* URL http://ocs.ciemat.es/EPS2015PAP/pdf/P4.120.pdf

[68] Quarteroni A, Sacco R and Fausto S 2007 *Numerical Mathematics* (Springer) URL http://www.springer.com/us/book/9783540346586